RESEARCH ARTICLE

INTERNATIONAL RESEARCH JOURNAL OF MULTIDISCIPLINARY TECHNOVATION

Asian Research Association

DOI: 10.54392/irjmt25319

Optimization of Ammonia Mixing in Selective Catalytic Reduction (SCR) Systems: A Computational Fluid Dynamics (CFD) Study on Swirl Angle and Mass Flow Rate Effects

Gutti Lokesh Kalyan [a,*], Rajendra Singh Rajput [a], Sunkara Srinivasa Rao [b], Mukesh Kumar Pandey [c]

[a] Department of Mechanical Engineering, ITM University, Gwalior, 474001, Madhya Pradesh, India

[b] Department of Electronics and Communication Engineering, Koneru Lakshmaiah Education Foundation, Bowrampet, Hyderabad, 500043, Telangana, India

[c] Department of Civil Engineering, ITM University, Gwalior, 474001, Madhya Pradesh, India

* Corresponding Author Email: lokeshkalyangutti@gmail.com

DOI: https://doi.org/10.54392/irjmt25319

Received: 03-03-2025; Revised: 06-05-2025; Accepted: 12-05-2025; Published: 23-05-2025

Abstract: The research deals with design a Heat Recovery Steam Generator (HRSG) model through Computational Fluid Dynamics (CFD) to evaluate Selective Catalytic Reduction (SCR) deNO_x procedures that help maintain sustainable environmental emissions. We study six swirl angles ranging from θ = 10° to θ = 60° at the GT diffuser exit to determine how they affect ammonia (NH_3) mixing before the SCR catalyst bed. The evaluation process occurred under mass flow conditions of 350 kg/s and 700 kg/s. Ammonia mixing uniformity must comply with Industrial standards by keeping the RMS value of mole fraction distribution less than 5% according to manufacturer specifications. The results indicate that a swirl angle of 30° produces the best NH_3 mixing performance with RMS 4.27% and theta = 40° provides the best temperature distribution ranging within ±7.41°C. The research delivers vital information regarding SCR system optimization when operational parameters change.

Keywords: Selective Catalytic Reduction (SCR), Swirl Angle θ, Gas Turbine (GT) diffuser, Ammonia (NH_3) mixing

1. Introduction

The control and reduction of nitrogen oxide (NOx) emissions forms a vital part in air pollution management that originates from industrial fuel combustion especially in coal-fired power plants. SCR stands among post-combustion technologies as an efficient solution because it fulfills stricter environmental requirements and operates with high effectiveness and meets wide scalability needs.

The combustion of fossil fuels in industrial facilities such as coal-fired power plants produce NOx emissions that represent a significant factor in air pollution and environmental decline [1]. Environmental regulations are becoming stricter worldwide which forces industries to establish strong emission control strategies according to [2]. SCR technology efficiently converts NOx in flue gas into nitrogen and water by injecting ammonia (NH_3) over a catalyst [3, 4].

SCR systems face three key operational challenges as non-uniform reagent dispersion, ammonia slip leading to catalyst deterioration, and suboptimal flow patterns [5]. The success of SCR systems depends heavily on achieving balanced distribution of NH_3 and NOx across the catalyst area. Studies confirm that improving flow dynamics mostly at reactor entrances represents a crucial step for enhancing denitrification outcomes [6, 7]. Computational Fluid Dynamics (CFD) serves as a primary analysis technology which enhances turbulent flow comprehension and improves reactant mixing capability by allowing design modification assessment of guide vanes and static mixers [8]. LES advances along with other advanced simulation methods enable researchers to achieve better understanding of complex flow reactions inside SCR reactors thus enabling more effective SCR system optimization [9].

The investigation of dynamic ammonia injection methods using instantaneous NOx flux distribution for more efficient SCR operation under diverse working conditions stands as one of the key recent findings [10]. The system efficiency improves when these approaches enable precise adjustments of the NH_3/NOx ratio which leads to reduced ammonia slip. The incorporation of intelligent control systems provides multiple advantages during power plant load changes and environmental

control implementations. Time Mixer and ensemble learning as machine learning models have demonstrated superior performance in NOx emission prediction according to [11, 12].

Effective SCR optimization requires proper regulation of the NH_3/NOx molar ratio inside the catalyst layer. The denitrification efficiency increases significantly when researchers enhance the uniformity of NH_3 distribution according to Ammonia Distribution [13]. Intelligent control systems of ammonia injection grid (AIG) have been developed to use the least ammonia while minimizing operational disruptions such as ammonium bisulfate formations [14]. Research has demonstrated that static mixing devices placed within SCR reactors raise both NH_3 and flue gas mixing performance and improve droplet evaporation rates [15, 16]. The design feature of zonal ammonia injection changes ammonia flow rates according to NOx variations in order to enhance SCR system performance [17].

The design of the SCR system catalyst plays a major role in determining overall system performance. Research evidence confirms that arranging the catalyst in multi-layered cross-channel structures results in superior denitrification efficiency together with reduced ammonia slip [18, 19]. Despite being a problem, catalyst degradation mainly due to uneven ash deposition remains a major operational challenge [20]. The growing number of CFD-based research studies identified particle movement irregularities which provided fundamental knowledge for developing approaches to extend catalyst operational life and minimize wear [21]. The study by [22] presented numerical findings about two-phase gas-liquid cylindrical flow which provides knowledge that researchers can adjust to fortify SCR catalyst channels against ash accumulation. The long-term effectiveness requires stable NH_3/NOx ratios and constant temperature at the reactor inlet as catalyst poisoning processes become active [23, 24].

The problem of catalyst poisoning from sulfur dioxide (SO_2) and hydrocarbon gases received attention in new research developments. The introduction of CeO_2 receptor onto V_2O_5-WO_3/TiO_2 surface produces increased removal of NOx in the presence of contaminant species thus improving the durability of SCR systems [25]. The template method used for high-Silica zeolite (high-Si) MER zeolite catalyst synthesis produces catalysts with improved water resistance besides achieving better NOx removal in SCR which validates high-Silica zeolite as a future-oriented SCR catalyst material [26].

The application of SCR advances beyond power plants because researchers focus on waste-to-energy technologies which utilize affordable polymer-based approaches for NOx elimination [27]. Researchers are conducting studies about using non-catalytic reduction methods with polymer-based systems to find economical solutions for NOx removal from waste-to-energy processes [27]. NOx control technologies have evolved through these systems to demonstrate how industrial operators implement flexible systems across different industrial applications. The researcher [28] found that numerical models of spray combustion showed fuel injection patterns are key factors in forming NOx during simulations which help optimize engine conditions before SCR systems. The evolution of NOx control technologies can be seen in these developments while showing that industrial operators are moving toward flexible systems in various industrial applications. The development of low-load combustion characteristics for coal-fired boiling systems has created new methods to enhance SCR performance according to [29]. Several difficulties involving lower flue gas temperatures and rising NOx levels at part load conditions encouraged researchers to explore alternative burner systems and operational adjustments that would improve SCR output and responsiveness.

SCR technology performs alongside biomass co-firing at Chinese coal-fired power plants as a solution for carbon reduction and NOx removal [30]. The introduction of biomass as a power plant coal replacement material creates important reductions in CO_2 emissions which align with international sustainability requirements.

Research teams have extensively studied SCR reactor structures for improving uniform flow and operational performance. The placement strategy combined with static mixers successfully distributed ammonia across the system according to [31]. The CFD simulations evaluated hybrid grids combined with guide vanes to enhance both velocity uniformity and intensity distribution in system [32]. Guide plates with innovative mixer configurations produced distributed flow patterns which led to raised NOx conversion performance [33].

Design and optimization efforts for SCR systems require essential application of CFD modeling as a fundamental tool. Hybrid LES-RANS delivers essential information to analyze droplet evaporation together with mixing processes for high pressure urea applications [34]. The investigation by [35] of mixed convection in trapezoidal cavities advanced fundamental knowledge about SCR reactor optimization by showing how to enhance both flow uniformity and heat transfer features. Engineers have discovered that SCR performance strengthens through multi-hole nozzles because these nozzles create preferred mixing realities that occur earlier than single-hole configurations [36]. Experimental investigations confirmed optimized results from studies which tested hybrid grid structure combinations and gate leaf construction plans through computational fluid dynamics modeling to enhance flow field distribution equality and denitrification performance outcomes [37].

The research behind ammonia distribution for SCR systems requires analysis of numerous concepts that extend beyond initial perception because it involves turbine operation and exhaust motion characteristics. Gas turbine efficiency is affected by multiple heat-based parameters as described by [38]. Exhaust manifold design investigations required researchers to study thermal stress and exhaust system material properties as essential elements which affect emission control. The researcher [39] points out that designers need to handle these factors appropriately in creating exhaust manifolds.

Rubber technologies have made recent developments to achieve homogeneous flow distribution while reducing system operational inefficiencies. The importance of optimizing ammonia injection together with mixing methods for this type of system is a primary focus of research [40]. The research by [41] introduced smart control systems to adjust both NOx slips level and NH_3 to NOx ratios. The combination of advanced CFD methods with experimental testing has produced significant advancements in designing and optimizing SCR systems according to [42].

Research examines how six different swirl angles (θ = 10°, 20°, 30°, 40°, 50°, and 60°) at GT diffuser exit affect SCR system functionality. This process handles problems that would be difficult when processing non-uniform flow patterns and achieving precise NH_3/NOx ratios for generating key NH_3 while maintaining flue gas quality and catalyst effectiveness. The study used CFD to process new topological advantages identified through previous work by building better flow homogeneity together with enhanced denitrification efficiency along with optimized diffuser-system interactions when operating under swirling conditions. The wide research on Selective Catalytic Reduction (SCR) systems fails to fully explain how different swirl angles affect NH_3/NOx mixture consistency when flows vary from 350-700 kg/s at gas turbine diffuser outlets. Industrial analysis of swirl-induced turbulence optimization for large-scale applications has yet to be addressed since research only focused on static mixers and single working conditions. Industries prevent using advanced simulation techniques for routine processes due to their high processing costs even when employing LES. This research evaluates six swirl angle ranges from 10° to 60° based on industrial data [8, 9] to optimize the performance of NH_3 mixing at θ = 30° and thermal uniformity at θ = 40° with RMS 4.27% and ±7.41°C. The dual-flow validation methodology delivers working-specific SCR operating insights for practical market usage which establishes a connection between academic theory and industrial manufacturing applications.

This research work intends to conduct three main objectives. First, it quantifies the effects of swirl angles ranging from 10° to 60° on NH_3 distribution consistency. Secondly, it validates CFD outcomes with industrial requirements of RMS <5% and ±10°C temperature stability. Lastly, it determines the best Swirl angle 'θ' for SCR operational excellence across variable flow rates from 350 to 700 kg/s.

2. Materials and Methods

2.1 Computational CFD Geometry and Mesh

The three-dimensional Heat Recovery Steam Generator (HRSG) design of Figure 1 locates indispensable components that bridge Module #1, Module #2, the Selective Catalytic Reduction (SCR) system, Module #3, Module #4, Module #5 and connects them with the exhaust gas inlet and stack. Exhaust gas inlet and stack receive visual representation along with flow direction indications in Figure 1.

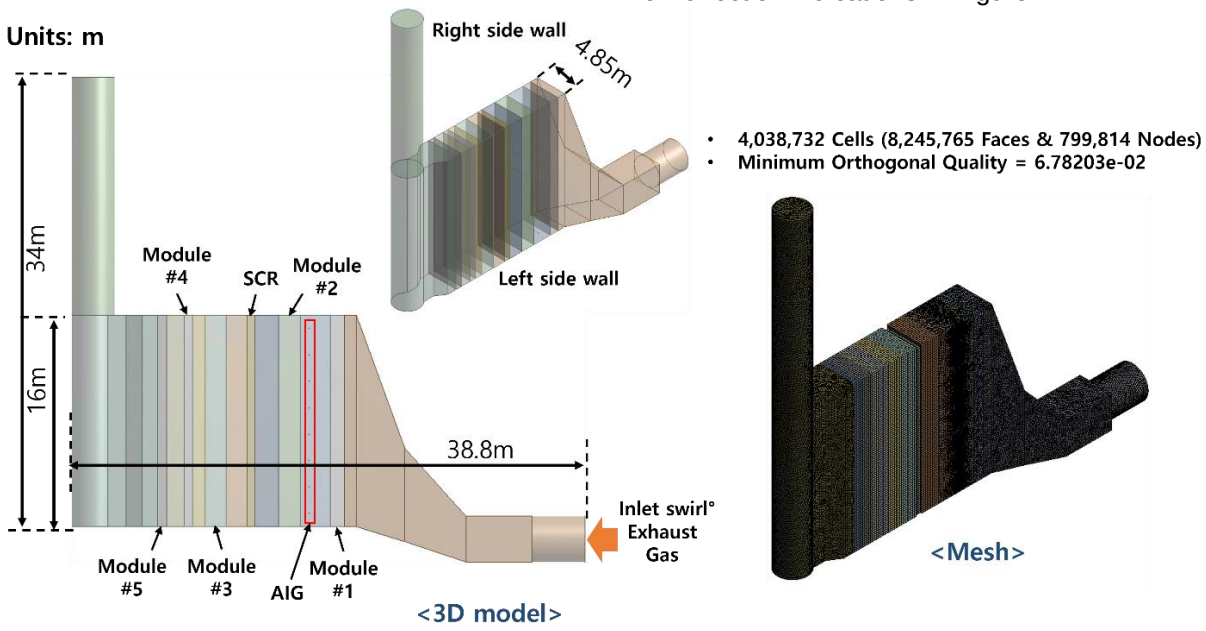

Figure 1. 3D model and its corresponding mesh for the HRSG

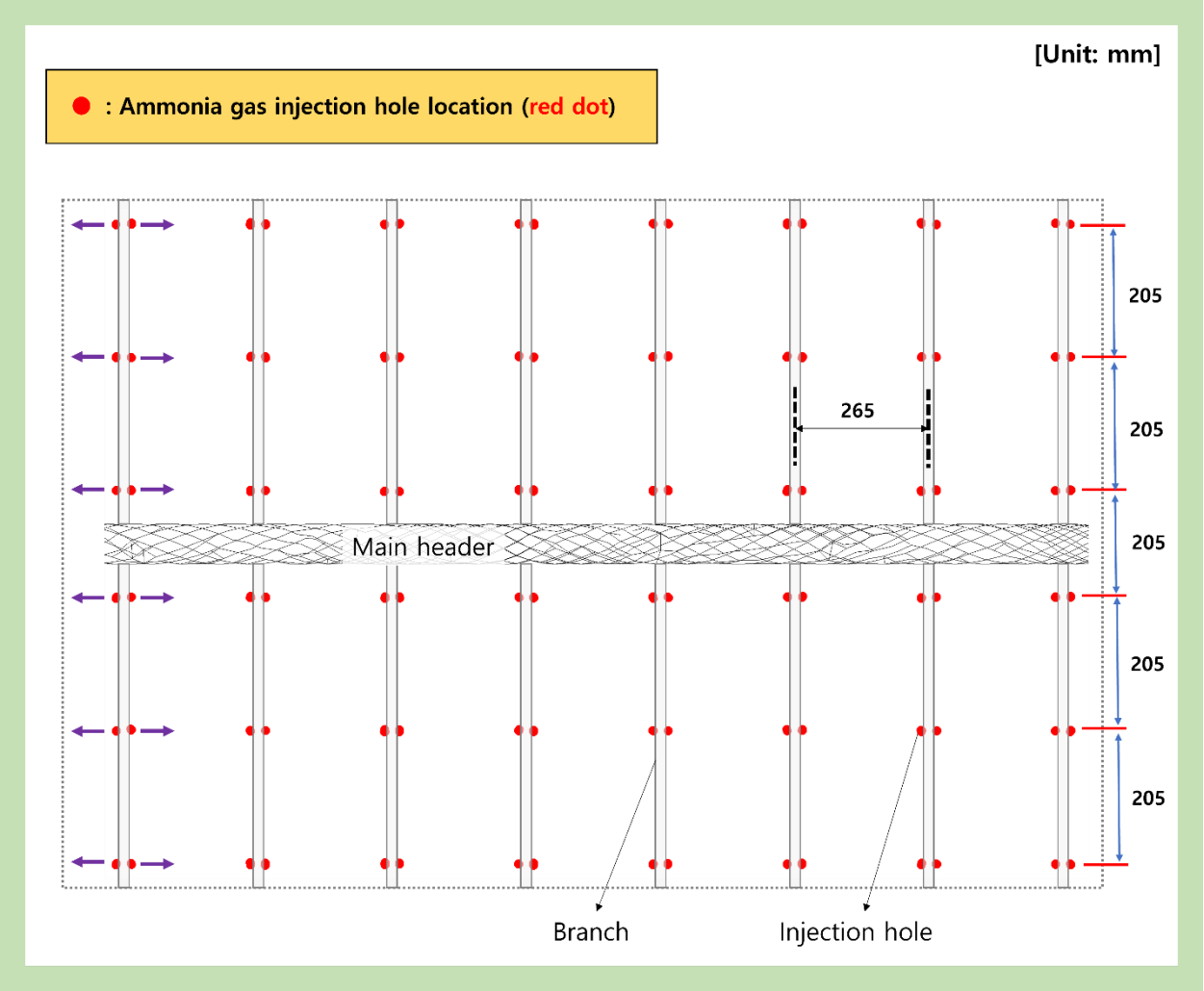

Figure 2. Optimal placement of ammonia injection holes and a typical AIG configuration

A diagnostic mesh with 4,038,732 cells provides this three-dimensional geometry with high-resolution computational capabilities. The computational accuracy and numerical stability to perform CFD analysis comes from a mesh orthogonal quality measurement of 6.78 × 10^{-2}.

The Ammonia Injection Grid (AIG) configuration (Figure 2) aligns with optimized designs from prior studies, where multi-point injection enhances NH_3/NOx mixing efficiency followed by Liu *et al.* 2019 [7], Sohn *et al.* 2021 [8] and Ye *et al.* 2018 [15]. Eight headers form the structure of Ammonia Injection Grid (AIG) as illustrated in Figure 2. The Ammonia Injection Grid consists of 2,882 injection openings, which are arranged with 265 mm between their branches and 205 mm between their vertical holes. The distance between the injection holes of the adjacent two branches amount to 245 mm. Through the entire 2,882 injection holes AIG delivers its intended function of enhancing NH_3 mixing. The technicians designed the branch distance to accommodate the thermal growth of the main header while achieving enough structural strength along with operational efficiency. The AIG design uses multiple injection points to improve the NH_3/NOx mixing process by structuring its layout according to flow dynamics as well as downstream turbulence patterns.

2.2 k-ε Turbulence Model

The realizable k-ε model (Eq. 1–2) was selected for its robustness in simulating turbulent flows in SCR systems, as demonstrated in similar studies by the authors Gao *et al.* 2019 [9], Kaario *et al.* 2017 [34]. This CFD analysis employed the realizable k-ε turbulence model, a widely utilized model for simulating turbulent flows. The relevant equations of governing turbulence quantities Eq. (1) and Eq. (2) are as follows:

$$\mu_t = \rho C_\mu \frac{k^2}{\varepsilon}, \; k_t = \frac{c_p \mu_t}{Pr_t}, \; D_t = \frac{\mu_t}{\rho Sc_t}$$

$$\frac{\partial(\rho k)}{\partial t} + \nabla \cdot (\rho \vec{v} k) = \nabla \cdot \left(\left(\mu + \frac{\mu_t}{\sigma_k} \right) \nabla k \right) + G_k + G_b - \rho\varepsilon - Y_M + S_k \quad (1)$$

$$\frac{\partial(\rho\varepsilon)}{\partial t} + \nabla \cdot (\rho \vec{v} \varepsilon) = \nabla \cdot \left(\left(\mu + \frac{\mu_t}{\sigma_\varepsilon} \right) \nabla \varepsilon \right) + C_{1\varepsilon} \frac{\varepsilon}{k} (G_k + C_{3\varepsilon} G_b) - C_{2\varepsilon} \rho \frac{\varepsilon^2}{k} + S_\varepsilon \quad (2)$$

In the realizable k-ε turbulence model, C_μ is a constant, k represents the turbulence kinetic energy and ϵ denotes the turbulence dissipation rate. The model also incorporates c_p, the heat capacity; Pr_t, the turbulent Prandtl number; and Sc_t, the turbulent Schmidt number. The turbulent Prandtl numbers for k and ϵ are represented by σ_k and σ_ϵ respectively. The dissipation rate in Eq. (3) $C_{1\varepsilon}$, $C_{2\varepsilon}$, and $C_{3\varepsilon}$ constants were also scaled using industrial data from industrial SCR units [8]. The terms G_k and G_b account for the generation of turbulence kinetic energy due to mean velocity gradients and buoyancy, respectively, while Y_M represents the contribution of fluctuating dilatation in compressible turbulence to the overall dissipation rate. Additionally, S_k and S_ε are user-defined source terms that allow customization of the model for specific applications. Together, these parameters and constants define the behavior of the realizable k-ε model in simulating turbulent flows.

2.3 Porous Media Model

The porous media model is utilized as a pressure loss source term in the momentum equation for the modules and SCR, formulated to account for both viscous and inertial pressure losses. The source term S_i , for the i-th momentum equation is expressed as

$$S_i = \nabla p = -\left(\sum_{j=1}^{3} D_{ij}\mu v_j + \sum_{j=1}^{3} C_{ij}\frac{1}{2}\rho|v|v_i\right) \quad (3)$$

where p denotes the static pressure, $v_j$represents the velocity in the j-direction, and $|v|$ is the magnitude of the velocity.

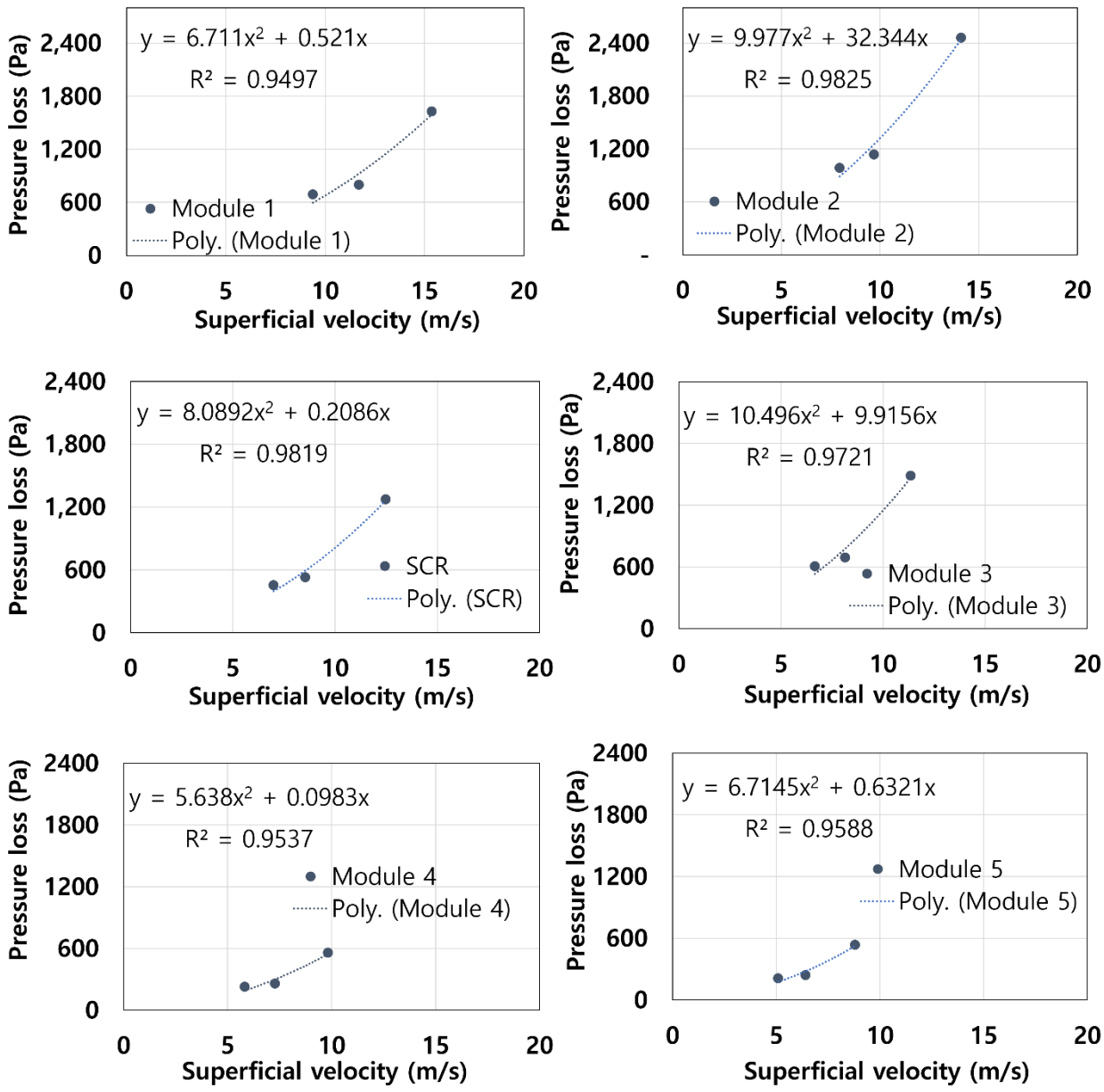

Figure 3. Correlation between superficial velocity and pressure loss in modules and SCR catalyst bed

The notations D_{ij} and C_{ij} in Eq. (3) are the coefficients obtained from experimental data [20, 33]. This method follows the same procedures as in [21] optimizing SCR reactor. Matrices for viscous and inertial pressure losses, respectively, μ is dynamic viscosity, and ρ is the fluid density. This model effectively captures pressure loss behavior within porous media by incorporating the combined effects of viscosity and inertial resistance. Figure 3 illustrates the quantitative relationship between superficial velocity and pressure loss across the modules and the SCR catalyst bed, providing insights into the system's flow dynamics.

2.4 Species Transport Equation

The conservation of mass applied to chemical species leads to the species transport equation (Eq. 4–6) incorporate turbulent Schmidt numbers Sc_t validated by Gao *et al.* 2019 [9] for SCR applications, which can be expressed as

$$\frac{\partial(\rho Y_i)}{\partial t} + \nabla \cdot (\rho \vec{v} Y_i) = -\nabla \cdot \vec{J}_i + R_i + S_i \quad (4)$$

In this equation Eq. (4), Y_i represents the mass fraction of species i, $\vec{J}_i$ is the diffusion flux of species i, R_i denotes the net rate of production of species i due to chemical reactions, and S_i accounts for the rate of creation of species i from other phases. The Eq. (5) diffusion flux $\vec{J}_i$ follows kinetic-theory-based models [2, 25].

$$\vec{J}_i = -\left(\rho D_{i,m} + \frac{\mu_t}{Sc_t}\right)\nabla Y_i - D_{T,i}\frac{\nabla T}{T} \quad (5)$$

where $D_{i,m}$ is the mass diffusion coefficient of species i in the mixture, Sc_t is the turbulent Schmidt number, μ_t is the turbulent viscosity is calculated using Eq. (1), and $D_{T,i}$ is the thermal diffusion coefficient of species i. The net rate of production of species i by chemical reactions is given as

$$R_i = MW_i \sum_{r=1}^{N_R} \hat{R}_{i,r} \quad (6)$$

where MW_i in Eq. (6) is the molecular weight of species i, and $\hat{R}_{i,r}$ represents the Arrhenius molar rate of creation or destruction of species i in reaction r. This equation comprehensively captures the transport and reaction dynamics of chemical species, including diffusion, turbulence, thermal effects, and chemical kinetics.

2.5 CFD Scheme and Solution Method

A steady-state, pressure-based segregated solver was employed for the simulation, utilizing the realizable k−ϵ turbulence model with a standard wall function. The Discrete Phase Model (DPM) simplified NH_3 injection simulations, reducing computational cost while preserving accuracy, as validated in [36]. Given that the small hole diameters, often measuring just a few millimeters, across thousands of injection points would generate tens to hundreds of millions of meshes in the computational domain, a direct CFD analysis of such geometry would be computationally impractical. As a solution, the DPM was used to simplify the gas-phase injection process, significantly reducing the required mesh count by abstracting the AIG shape. Additionally, the porous media model was employed to represent pressure losses in the modules and the SCR catalyst bed. The pressure loss source term in the momentum equation is expressed as:

$$S_i = -\left(\sum_{j=1}^{3} D_{ij}\mu u_j + \sum_{j=1}^{3} C_{ij}\frac{1}{2}\rho|u|u_j\right) \quad (7)$$

Where in Eq. (7) D_{ij} denotes the viscous resistance coefficient, and C_{ij} represents the inertial resistance coefficient. This approach balances computational efficiency and accuracy for the CFD analysis.

The energy transport within modules was modeled using a temperature-difference-based approach to handle the energy source (or sink) term (Eq. 8) was calibrated using design data from [31].

$$S_e = \frac{E}{V} = -h\left(T_{gas} - T_{solid}\right)A_{sp} \quad (8)$$

The energy sink term, S_e [W/m3], is defined based on the energy sink rate E [W], and the volume of the module V [m3]. The heat transfer process is governed by the heat transfer coefficient h[W/m^2.K], the gas-phase temperature T_{gas} [K], the solid-phase temperature T_{solid} [K], and the specific surface area of the module $A_{sp}[m^2/m^3]$. The parameters in Eq. (8) h, A_{sp} and T_{solid} are meticulously selected to ensure that the computational fluid dynamics (CFD) simulation results are consistent with the design values for the average temperature showed before and after the module.

2.6 Computational Details

In the present work, the inlet and outlet of the flue are set as mass flow inlet and pressure outlet, respectively, and the adiabatic no-slip boundary condition is applied to the walls and internals. We selected the direction specification method to generate swirl flow at the inlet, the Intensity and Hydraulic Diameter method is used to specify turbulence. The detailed boundary conditions are summarized in Table 1, provide validated CFD studies that define typical operating conditions for SCR systems in similar applications [8, 17].

Table 2 details the fluid properties used in the simulations, derived using models such as the incompressible-ideal-gas equation for density and mixing laws for specific heat and thermal conductivity. These parameters are integral for achieving accurate predictions of flow and heat transfer behaviors.

Table 1. Boundary Conditions for Simulation at Two Distinct Mass Flow Rates

Contents	Units	Case-1	Case-2
Swirl Angle	°	10, 20, 30, 40, 50, 60	10, 20, 30, 40, 50, 60
Exhaust Gas Flow Rate	kg/hr	1,260,000	2,520,000
	kg/s	350	700
Exhaust gas temperature	℃	650	650
Exhaust Gas Composition (at GT exit)			
-N2	vol%, wet	74.08	74.08
-O2	vol%, wet	11.33	11.33
-CO2	vol%, wet	4.43	4.43
-H2O	vol%, wet	9.27	9.27
-Ar	vol%, wet	0.89	0.89
Sum		100.00	100.00

Table 2. Fluid Properties

Contents	Units	Method
Density	kg/m^3	Incompressible-ideal-gas
Specific Heat	$J/kg.k$	Mixing-law
Thermal conductivity	$W/m.k$	Mass-weighted-mixing-law
Viscosity	$kg/m.s$	Mass-weighted-mixing-law
Mass Diffusivity	m^2/s	Kinetic-theory

Table 3. Conditions of the Injected AIG Reducing Gas

Cases	Reducing Agent	NH_3 Consumption	Extracted Flue Gas Volume Flow	Injection Gas Temperature
Case-1 & 2	Anhydrous NH_3	50.0 kg/hr	340 Am3/min@360.0℃	140.0℃

Table 3 outlines the specifications of the reducing agent injected through the AIG, including the mass flow rate (50 kg/hr), extracted flue gas volume (340 Am³/min), and injection gas temperature (140°C). Table 3 align with the authors Liu *et al.* 2019 [7] and Zhu *et al*. 2025 [17] research discuss optimal NH_3 injection strategies to ensure proper mixing and NOx reduction efficiency. The simulations were performed using ANSYS Fluent [43] to simulate the SCR deNOx process. The standard k−ϵ turbulence model coupled with the SIMPLE algorithm was employed to obtain a steady flow field. The simulation converged after 10,000 iterations.

2.7 Evaluation Index

The uniformity of velocity and the concentration of the reducing agent is quantified using the Root Mean Square (RMS) of the normal velocity and NH_3 mole fraction at a specific plane. The formula for RMS [6, 31] is expressed in Eq. (9) as follows:

$$RMS(\%) = \sqrt{\frac{\sum_{i=0}^{n}(x_i - x_0)^2}{n}}/x_0 \times 100 \text{ where } x_0 = \frac{\sum_{i=1}^{n} x_i}{n} \quad (9)$$

This evaluation index contains the specific variable x among its components alongside x_0 which stands for the average value of x across the designated plane. This evaluation index considers n sampling points as the number of CFD cells analyzed and x_i shows the variable values of individual cells on each plane. The research variables allow computation of Root Mean Square (RMS) percentage to evaluate uniformity in velocity distribution and mole fraction of NH_3. Temperature uniformity depends on the maximum deviation from typical average plane measurements

while uniformity of velocity comes from RMS values and NH_3 mole fraction assessment occurs through average measures. Performance monitoring with design assessments allows the evaluation of these metrics to determine systems' adequacy related to uniformity requirements for the HRSG and SCR devices. An examination of normal velocity and temperature uniformity needs to be conducted at both Inlet/Outlet regions of Module #1 and Module #2. Also check the normal velocity uniformity together with temperature and reducing agent concentration (mole fraction) uniformity at SCR catalyst bed inlet to validate design adequacy of the HRSG and SCR systems. The SCR catalyst vendor requires normal velocity to be under 15% uniformity while temperature must stay within ±10°C and reducing agent mole fraction does not exceed 5% according to their specification. The SCR system achieves its peak efficiency and performance by maintaining ideal flow conditions together with uniform temperature and reactants distribution because these standards lead to effective denitrification while adhering to emission regulations.

3. Results and Discussion

3.1 Validation of Energy Transport Parameters

The energy transport parameters (coefficients) within the modules, including T_{solid} and $h\,A_{sp}$, were identified through a trial-and-error method using the temperature design data before and after the modules.

Table 4. Parameters and Computational Fluid Dynamics (CFD) Results Associated with Energy Transfer Within Modules for Case-1

Swirl Angle	Module	T_{solid} (℃)	$h\,A_{sp}$ (W/m3-K)	Ave. Gas Temperature Before Module (℃)			Ave. Gas Temperature After Module (℃)		
				Design	CFD	(Diff.)	Design	CFD	(Diff.)
10°	Module #1	300	2,566.34	650	**650.00**	0.00%	540	**537.71**	0.42%
	Module #2	250	1,533.36	540	**537.71**	0.42%	450	**448.26**	0.39%
	Module #3	200	2,056.27	450	**448.26**	0.39%	355	**353.19**	0.51%
	Module #4	150	9,027.73	355	**353.19**	0.51%	240	**237.95**	0.85%
	Module #5	80	12,166.06	240	**237.95**	0.85%	130	**129.20**	0.62%
20°	Module #1	300	2,566.34	650	**650.00**	0.00%	540	**538.82**	0.22%
	Module #2	250	1,533.36	540	**538.82**	0.22%	450	**448.72**	0.28%
	Module #3	200	2,056.27	450	**448.72**	0.28%	355	**353.61**	0.39%
	Module #4	150	9,027.73	355	**353.61**	0.39%	240	**238.49**	0.63%
	Module #5	80	12,166.06	240	**238.49**	0.63%	130	**129.30**	0.54%
30°	Module #1	300	2,566.34	650	**650.00**	0.00%	540	**540.13**	-0.02%
	Module #2	250	1,533.36	540	**540.13**	-0.02%	450	**448.72**	0.28
	Module #3	200	2,056.27	450	**448.72**	0.28%	355	**354.15**	0.24%
	Module #4	150	9,027.73	355	**354.15**	0.24%	240	**239.16**	0.35%
	Module #5	80	12,166.06	240	**239.16**	0.35%	130	**129.17**	0.64%
40°	Module #1	300	2,566.34	650	**650.00**	0.00%	540	**540.51**	-0.09%
	Module #2	250	1,533.36	540	**540.51**	-0.09%	450	**449.67**	0.07%
	Module #3	200	2,056.27	450	**449.67**	0.07%	355	**354.42**	0.16%
	Module #4	150	9,027.73	355	**354.42**	0.16%	240	**239.44**	0.23%
	Module #5	80	12,166.06	240	**239.44**	0.23%	130	**129.43**	0.44%
50°	Module #1	300	2,566.34	650	**649.98**	0.00%	540	**540.27**	-0.05%
	Module #2	250	1,533.36	540	**540.27**	-0.05%	450	**450.06**	-0.01%
	Module #3	200	2,056.27	450	**450.06**	-0.01%	355	**354.72**	0.08%
	Module #4	150	9,027.73	355	**354.72**	0.08%	240	**239.72**	0.12%
	Module #5	80	12,166.06	240	**239.72**	0.12%	130	**129.67**	0.25%
60°	Module #1	300	2,566.34	650	**649.79**	0.03%	540	**539.78**	0.04%
	Module #2	250	1,533.36	540	**539.78**	0.04%	450	**450.36**	-0.08%
	Module #3	200	2,056.27	450	**450.36**	-0.08%	355	**354.92**	0.02%
	Module #4	150	9,027.73	355	**354.92**	0.02%	240	**239.83**	0.07%
	Module #5	80	12,166.06	240	**239.83**	0.07%	130	**129.74**	0.20%

Table 5. Parameters and Computational Fluid Dynamics (CFD) Results Associated with Energy Transfer Within Modules for Case-2

Swirl Angle	Module	T_{solid} (℃)	$h\ A_{sp}$ (W/m3-K)	Ave. Gas Temperature Before Module (℃)			Ave. Gas Temperature After Module (℃)		
				Design	CFD	(Diff.)	Design	CFD	(Diff.)
10°	Module #1	300	5,136.45	650	**649.99**	0.00%	540	**537.57**	0.45%
	Module #2	250	3,075.44	540	**537.57**	0.45%	450	**448.58**	0.31%
	Module #3	200	4,113.06	450	**448.58**	0.31%	355	**352.91**	0.59%
	Module #4	150	17,689.03	355	**352.91**	0.59%	240	**238.50**	0.63%
	Module #5	80	23,929.96	240	**238.50**	0.63%	130	**129.32**	0.52%
20°	Module #1	300	5,136.45	650	**650.00**	0.00%	540	**538.52**	0.27%
	Module #2	250	3,075.44	540	**538.52**	0.27%	450	**449.00**	0.22%
	Module #3	200	4,113.06	450	**449.00**	0.22%	355	**353.30**	0.48%
	Module #4	150	17,689.03	355	**353.30**	0.48%	240	**239.01**	0.41%
	Module #5	80	23,929.96	240	**239.01**	0.41%	130	**129.86**	0.11%
30°	Module #1	300	5,136.45	650	**650.00**	0.00%	540	**539.75**	0.05%
	Module #2	250	3,075.44	540	**539.75**	0.05%	450	**449.49**	0.11%
	Module #3	200	4,113.06	450	**449.49**	0.11%	355	**353.71**	0.36%
	Module #4	150	17,689.03	355	**353.71**	0.36%	240	**239.48**	0.22%
	Module #5	80	23,929.96	240	**239.48**	0.22%	130	**129.33**	0.51%
40°	Module #1	300	5,136.45	650	**650.00**	0.00%	540	**540.08**	-0.01%
	Module #2	250	3,075.44	540	**540.08**	-0.01%	450	**449.75**	0.06%
	Module #3	200	4,113.06	450	**449.75**	0.06%	355	**353.87**	0.32%
	Module #4	150	17,689.03	355	**353.87**	0.32%	240	**239.52**	0.20%
	Module #5	80	23,929.96	240	**239.52**	0.20%	130	**129.30**	0.54%
50°	Module #1	300	5,136.45	650	**649.98**	0.00%	540	**539.74**	0.05%
	Module #2	250	3,075.44	540	**539.74**	0.05%	450	**450.22**	-0.05%
	Module #3	200	4,113.06	450	**450.22**	-0.05%	355	**354.33**	0.19%
	Module #4	150	17,689.03	355	**354.33**	0.19%	240	**240.17**	-0.07%
	Module #5	80	23,929.96	240	**240.17**	-0.07%	130	**129.97**	0.03%
60°	Module #1	300	5,136.45	650	**649.79**	0.03%	540	**539.21**	0.15%
	Module #2	250	3,075.44	540	**539.21**	0.15%	450	**450.49**	-0.11%
	Module #3	200	4,113.06	450	**450.49**	-0.11%	355	**354.53**	0.13%
	Module #4	150	17,689.03	355	**354.53**	0.13%	240	**240.32**	-0.13%
	Module #5	80	23,929.96	240	**240.32**	-0.13%	130	**130.07**	-0.05%

The data are summarized in Table 4 and Table 5, the selected parameters and the corresponding temperature results. While Figure 4 illustrates the inspection planes were adapted from [8] to ensure reproducibility for the area-weighted average temperature, the discrepancies between the CFD results and the design data were within approximately 1.0% for both Case-1 and Case-2. This close agreement validates the accuracy of the energy transport parameters and the computational approach used in this study.

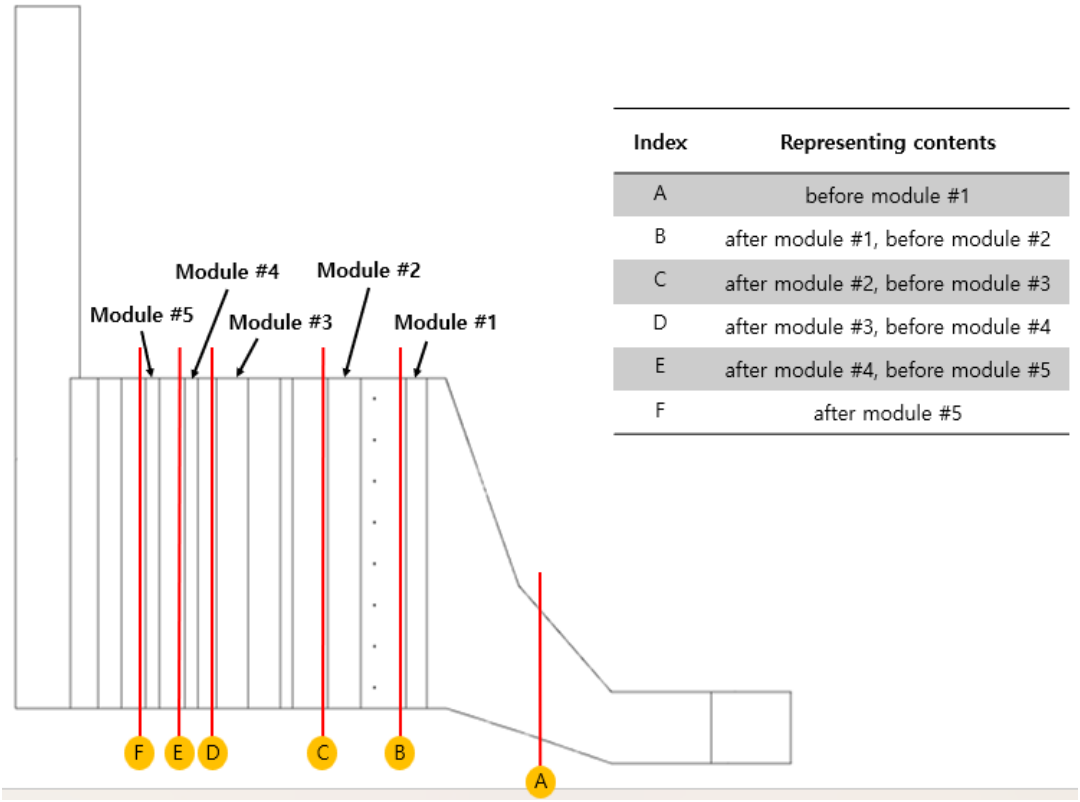

Index	Representing contents
A	before module #1
B	after module #1, before module #2
C	after module #2, before module #3
D	after module #3, before module #4
E	after module #4, before module #5
F	after module #5

Figure 4. Inspection planes for area-weighted average temperature upstream and downstream of modules

3.2 Contours of Static Pressure and Z-Velocity Pathlines

The contours of static pressure (Pa) for different swirl angles (θ = 10º, 20º, 30º, 40º, 50º, and 60º) are presented in Figures 5–7. Specifically, Figure 5 illustrates the static pressure distribution for θ = 10º and 20º, Figure 6 for θ = 30º and 40º and Figure 7 for θ = 50º and 60º.

The average static pressure at the Heat Recovery Steam Generator (HRSG) inlet varies for each case, while the outlet pressure remains at 0 Pa. A constant ambient pressure of 101,325 Pa was maintained throughout the analysis. Additionally, the static pressure distribution across all modules, from Module #1 to Module #5, is depicted.

The z-velocity (m/s) pathlines from the HRSG inlet for different swirl angles, the results showed in Figures 8–10. Specifically, Figure 8 showed the pathlines for θ = 10º and 20º, Figure 9 for θ = 30º and 40º and Figure 10 for θ = 50º and 60º.

These visualizations provide insights into the flow characteristics and velocity distribution within the HRSG for different swirl configurations. The high-velocity exhaust gas from the gas turbine (GT) exit primarily impacts the lower section of the HRSG. As it encounters the pressure resistance of Module #1, the flue gas begins to spread upward toward the upper section. As the flow progresses through Modules #2 to #5, the distribution gradually becomes more uniform.

3.3 Analysis of Velocity and Temperature Distribution

Research groups performed extensive examinations of HRSG Heat Recovery Steam Generator velocity and temperature distributions for the purposes of achieving Selective Catalytic Reduction (SCR) system optimal performance under uniform flow and thermal conditions. In this research work Case-1 (m = 350 kg/s) is presented in detail along with Case-2 (m = 700 kg/s). The research displays Case-1 data via visual components but includes comprehensive tables for both case conditions. Different mass flow rates serve two functions in the research as they affect system flow patterns and thermal distribution behavior to establish essential operational knowledge about HRSG and SCR systems.

3.3.1 Velocity Distribution

Velocity contours for Case-1 the results showed in Figures 11–13 at the HRSG center plane and Module #1 inlet and Module #2 inlet and SCR inlet. Tables 6 and 7 provide information about the z-velocity Root Mean Square value which measures velocity distribution uniformity for both Case-1 and Case-2.

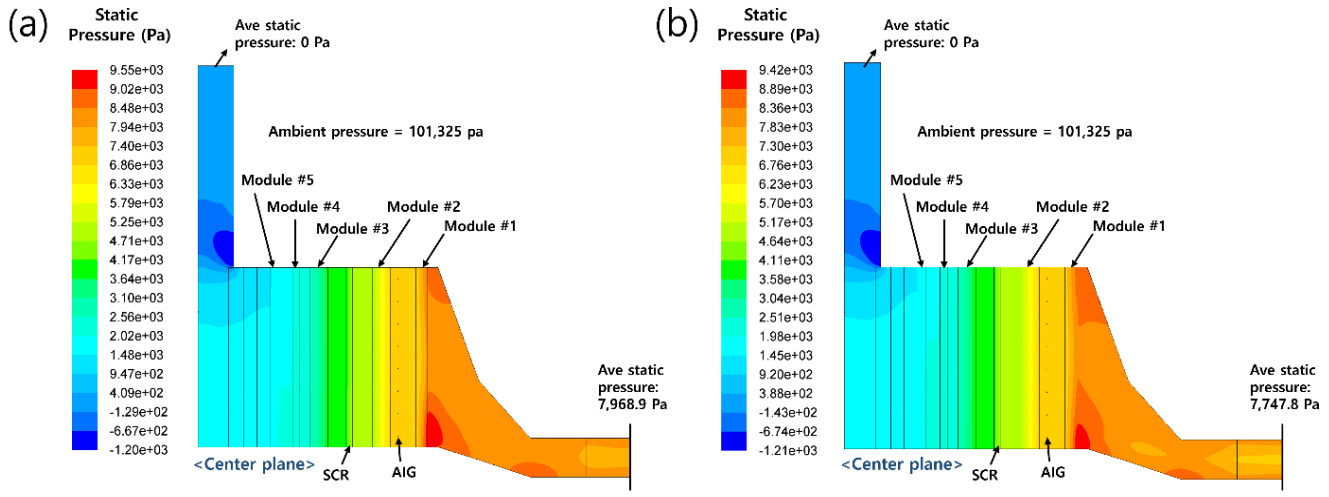

Figure 5. Static pressure at the center plane of the HRSG for (a) θ = 10º; (b) θ = 20º

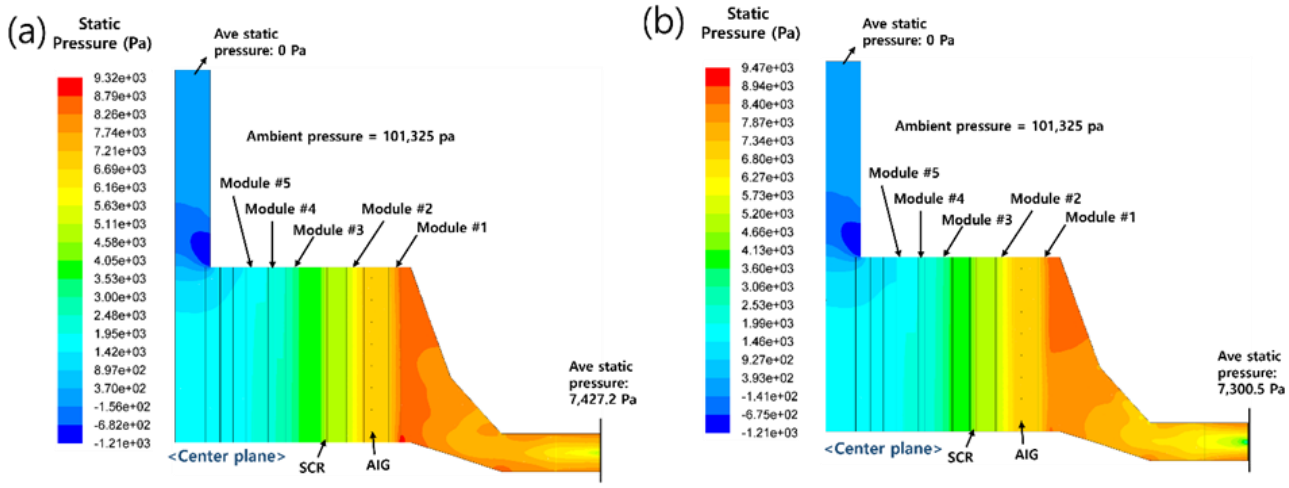

Figure 6. Static pressure at the center plane of the HRSG for (a) θ = 30º; (b) θ = 40º

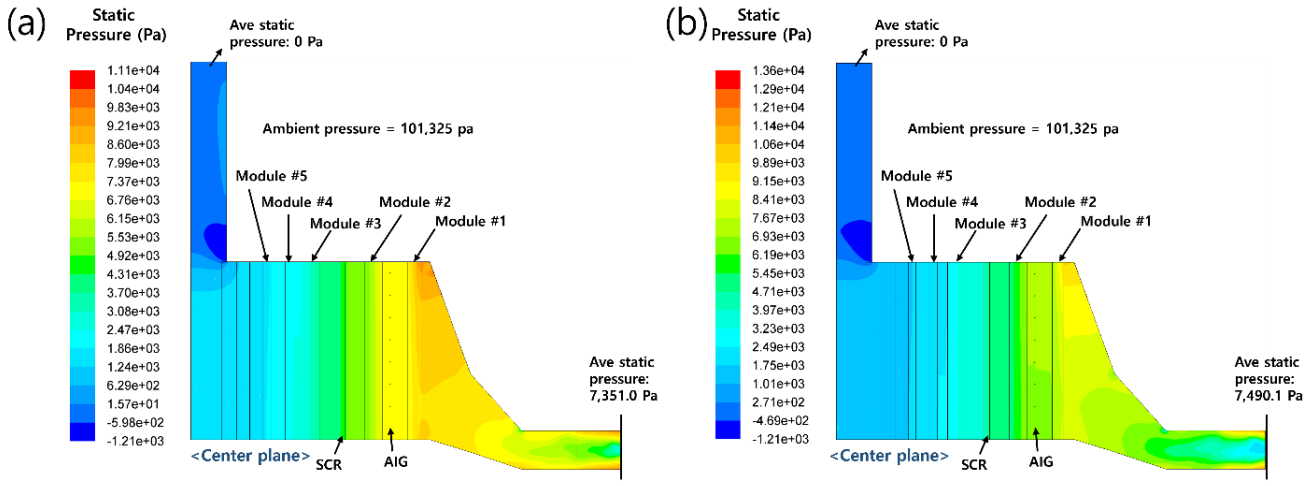

Figure 7. Static pressure at the center plane of the HRSG for (a) θ = 50º; (b) θ = 60º

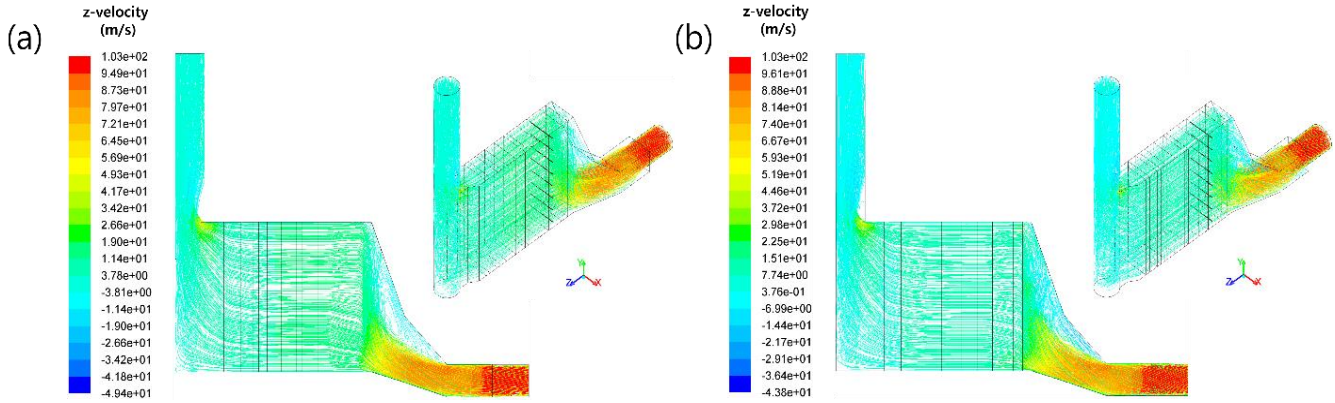

Figure 8. Pathlines from the HRSG inlet highlighted by z-velocity distribution for (a) θ = 10º; (b) θ = 20º

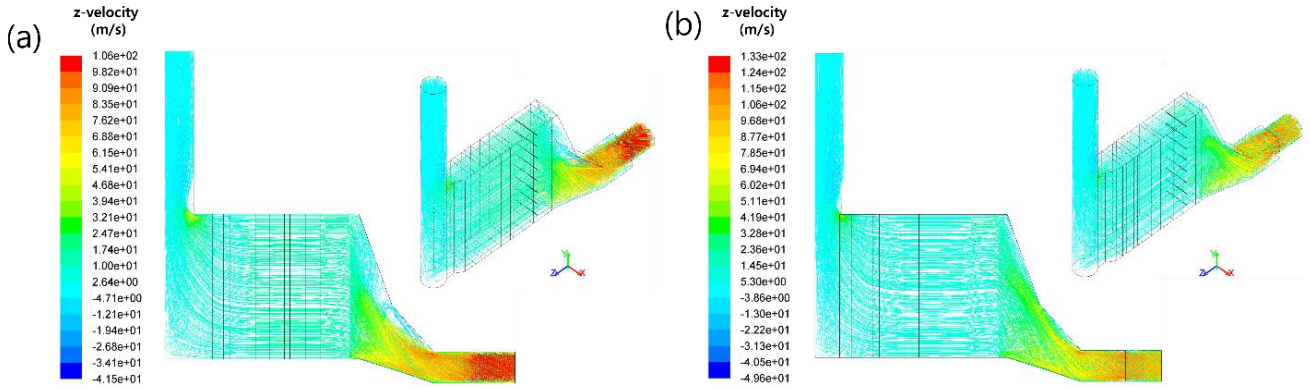

Figure 9. Pathlines from the HRSG inlet highlighted by z-velocity distribution for (a) θ = 30º; (b) θ

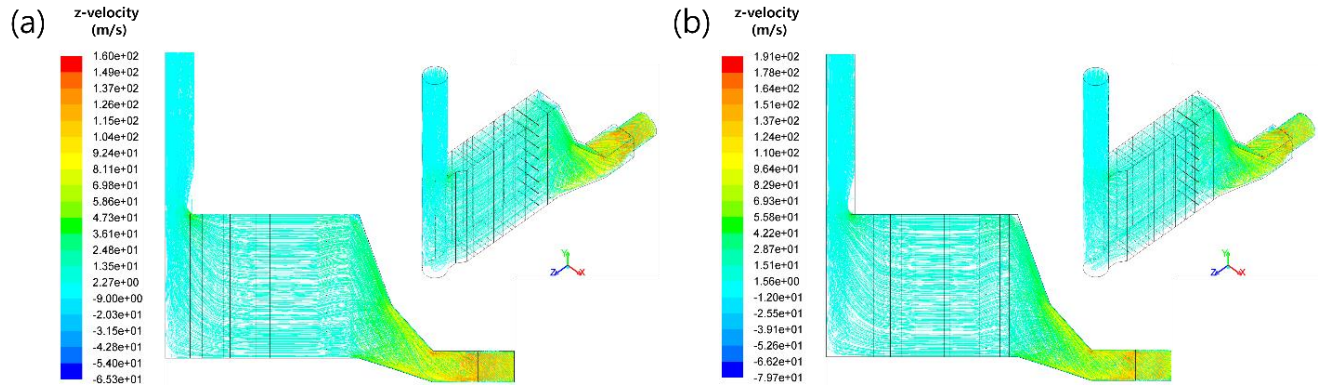

Figure 10. Pathlines from the HRSG inlet highlighted by z-velocity distribution for (a) θ = 50º; (b) θ = 60º

At Module #1 inlet the RMS of z-velocity shows substantial deviation from 25.80% (θ=10°) to 29.73% (θ=60°) in Case-2. The maximum RMS value that occurs at θ = 60° (29.73%) reflects separation of flow due to intense swirl which generates slow-moving recirculation zones that disrupt the momentum transfer. The RMS reaches its minimum point of 19.02% when the angle is set to 30° because this swirl strength maintains flux stability much like Sohn *et al.* 2021 [8] results found in practical SCR. The fluid flow displays unstable patterns whenever swirl angles surpass 30° nevertheless it fails to create proper mixing when the swirl angle remains at 10°. The RMS of z-velocity showed an identical variation at Module #1 inlet between θ = 10° to θ = 60° where it starts at 25.80% before reaching 29.73%. This pattern corresponds with Case-1 results. The SCR inlet showed low z-velocity RMS values below 1.19% which meeting industrial standards [8, 15, 32] across all investigated swirl angles because the higher mass flow does not impact velocity distribution uniformity at this critical point. Under greater mass flow conditions, the HRSG design operates effectively to preserve its flow dynamics capability.

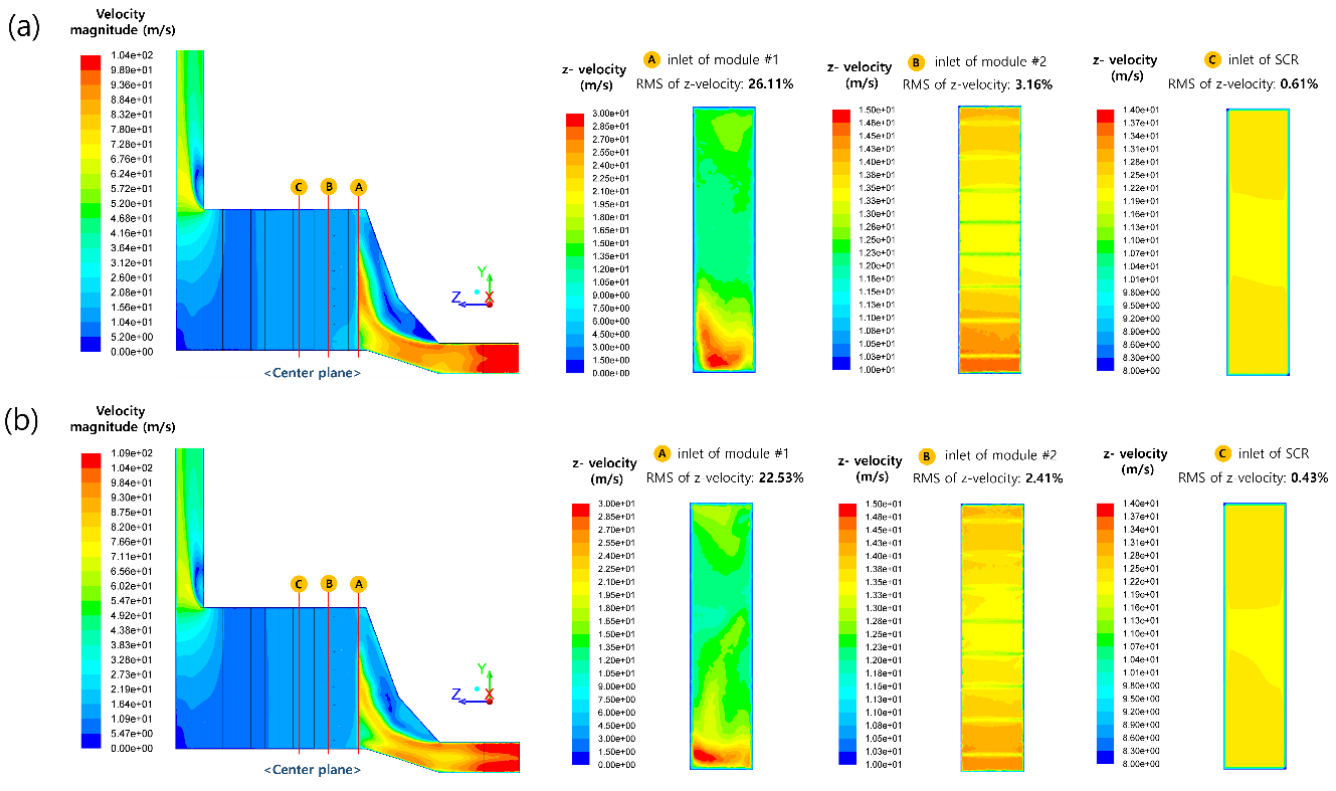

Figure 11. Velocity contours (magnitude and z-velocity) at the HRSG center plane, Module #1 inlet, Module #2 inlet, and SCR inlet for (a) θ = 10º; (b) θ = 20º

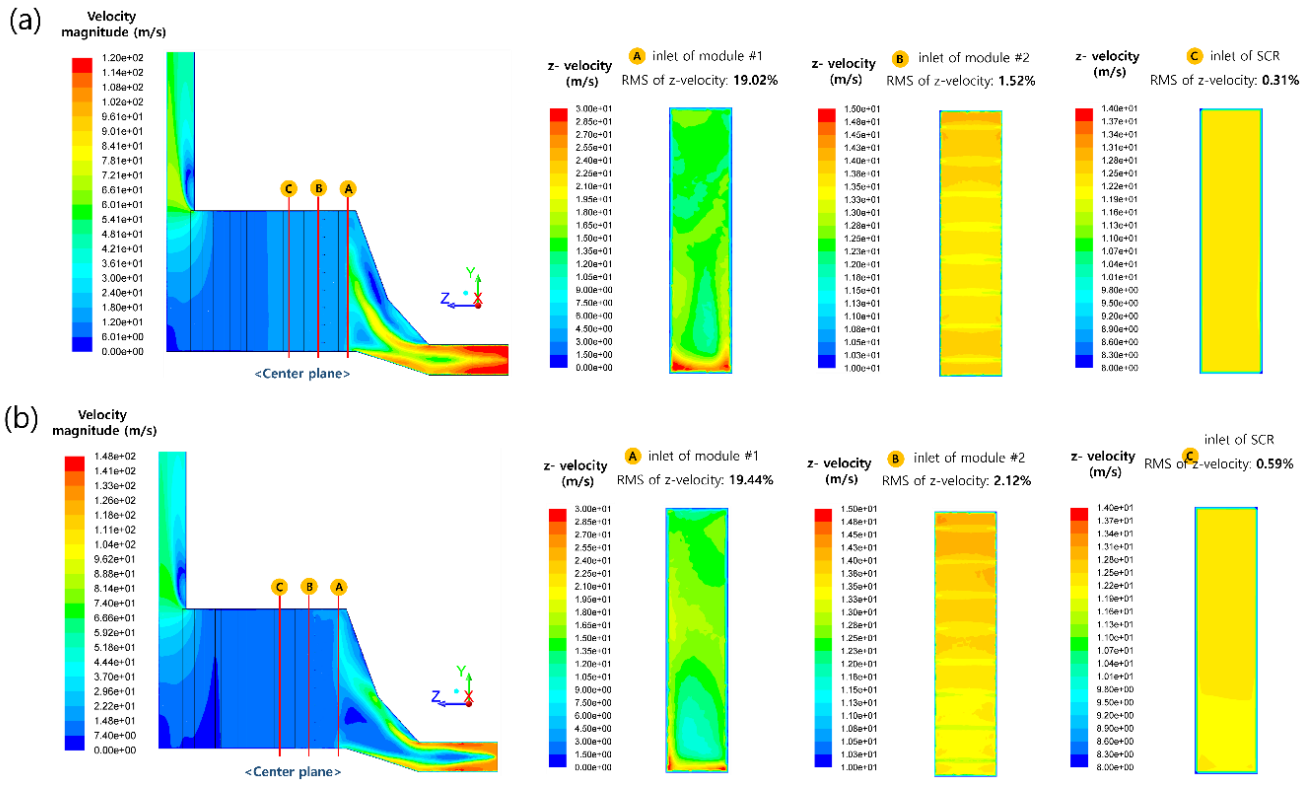

Figure 12. Velocity contours (magnitude and z-velocity) at the HRSG center plane, Module #1 inlet, Module #2 inlet, and SCR inlet for (a) θ = 30º; (b) θ = 40º

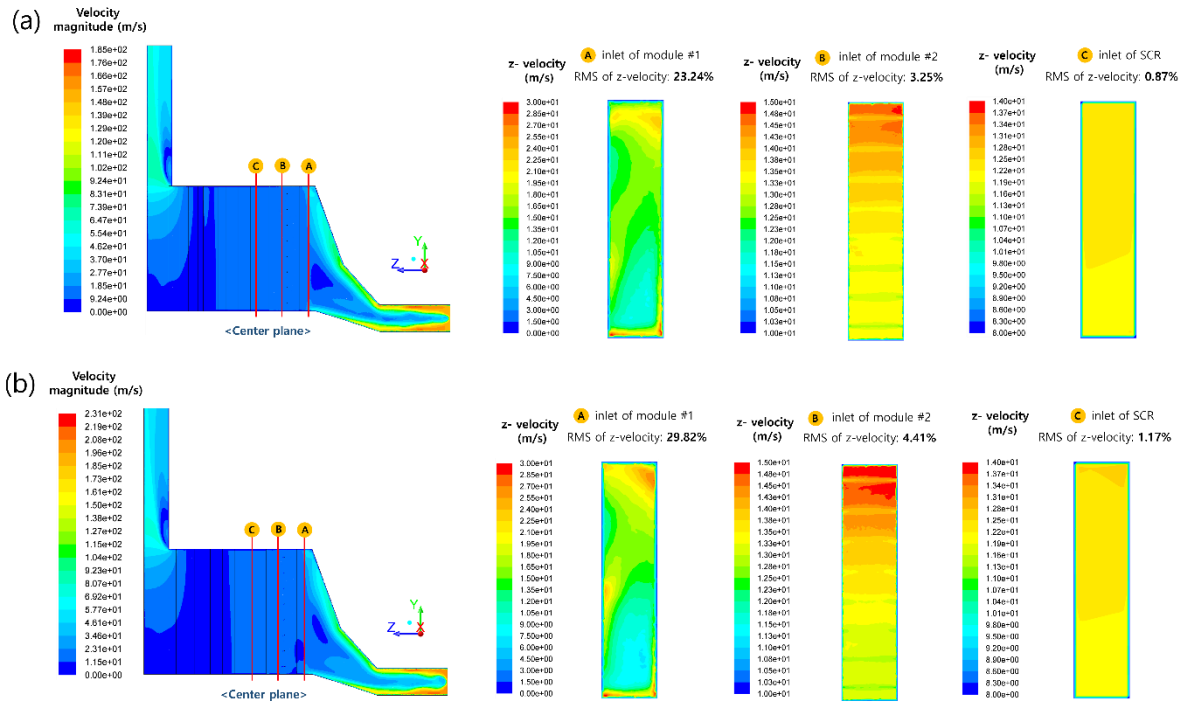

Figure 13. Velocity contours (magnitude and z-velocity) at the HRSG center plane, Module #1 inlet, Module #2 inlet, and SCR inlet for (a) θ = 50º; (b) θ = 60º

3.3.2 Temperature Distribution

The temperature distribution data at the center plane of HRSG Module #1 inlet and SCR inlet and at Module #2 inlet is presented through Figures 14–16 under Case-1 conditions. The maximum temperature differences represent the measurement of uniform temperature distribution and these values appear in Tables 8 and 9 for both Case-1 and Case-2.

The inlet temperature difference of Module #1 reaches a maximum value of 16.64°C when θ equals 10° and a minimum value of 30.04°C when θ equals 60° for Case-1. The temperature distribution becomes more uniform across the flow direction as the modules receive the stream so the maximum temperature difference at the SCR inlet reaches below 20.26°C across all swirl angles. When the system operates at θ = 40° the SCR inlet temperature difference stays within the acceptable range [5, 24] of ±10°C.

The catalyst bed benefits from improved convective heat transfer because of secondary flows that form at θ = 40°. The SCR performance can sustain over long periods due to the absence of hot spots which protect the catalyst from entering Ye *et al.* 2021 [5]. Thermal homogenization gets optimal at θ = 40° because this angle maintains proper swirl mixing. However, the high turbulence of θ = 60° increases temperature gradients.

The inlet temperature variation of Module #1 throughout Case-2 spans from 14.44°C at θ = 10° up to 27.03°C at θ = 60°. All swirl angles maintain a maximum temperature difference of less than 21.85°C at the SCR inlet as the flow progresses across the HRSG until reaching uniform temperature distribution. The success of SCR performance depends heavily on proper optimization of swirl angles to maintain necessary temperature uniformity. Description findings demonstrate the HRSG design's ability to regulate thermal variations across mass flow rates, however the required operational specifications can only be met at the SCR entrance when the system operates at θ = 40°.

3.4 Analysis of NH_3 Mole Fraction Distribution

Ammonia (NH_3) distribution uniformity plays an essential role in maintaining effective operation of Selective Catalytic Reduction (SCR) systems. Research conducted ammonia mole fraction distribution rates at the Ammonia Injection Grid (AIG) and both ends of Module #2 and the entrance of the SCR catalyst bed. The findings include both Case-1 for 350 kg/s and Case-2 for 700 kg/s together with visual representations for Case-1 and comprehensive tabulated outcomes for both cases. Multiple Figures 17 through 19 show the distribution of NH_3 mole fractions at multiple inspection positions within the HRSG to demonstrate the effects of different swirl angles on NH_3 blending.

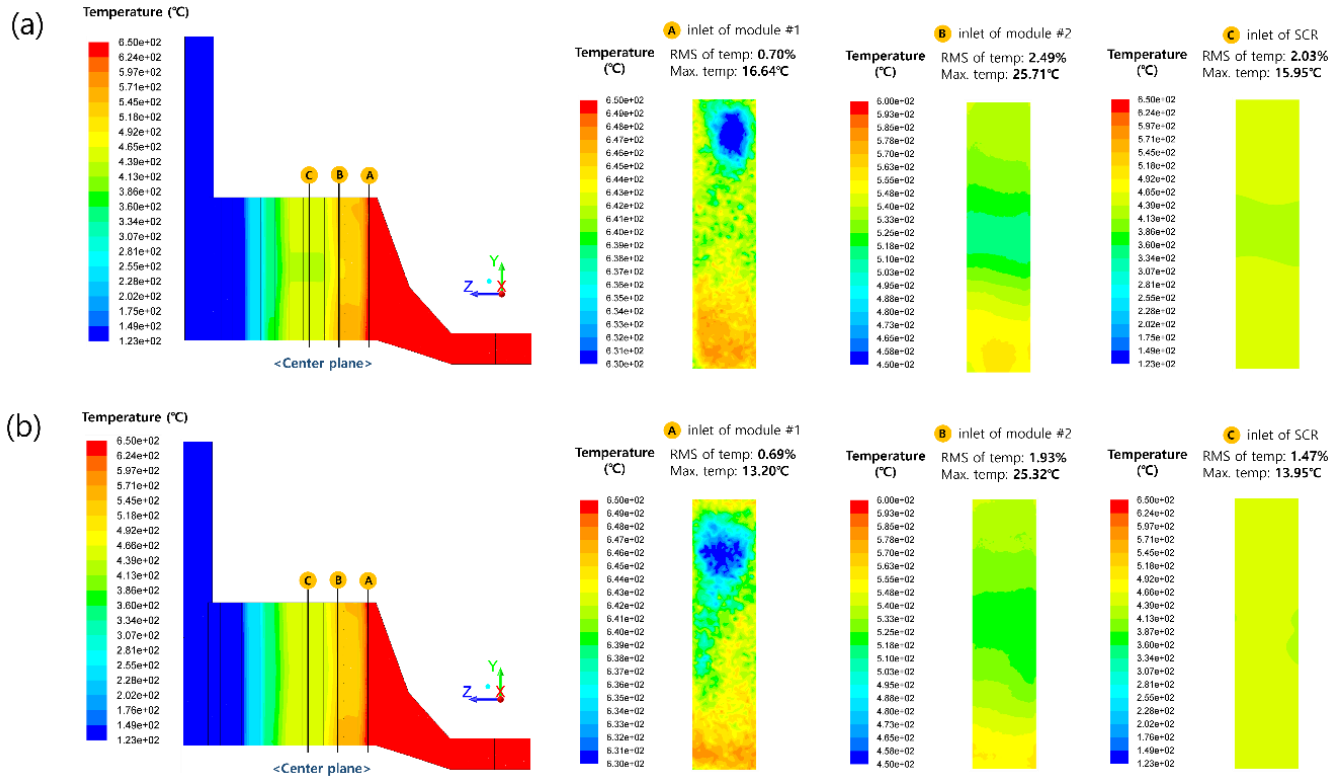

Figure 14. Temperature contours at the HRSG center plane, Module #1 inlet, Module #2 inlet, and SCR inlet for (a) θ = 10º; (b) θ = 20º

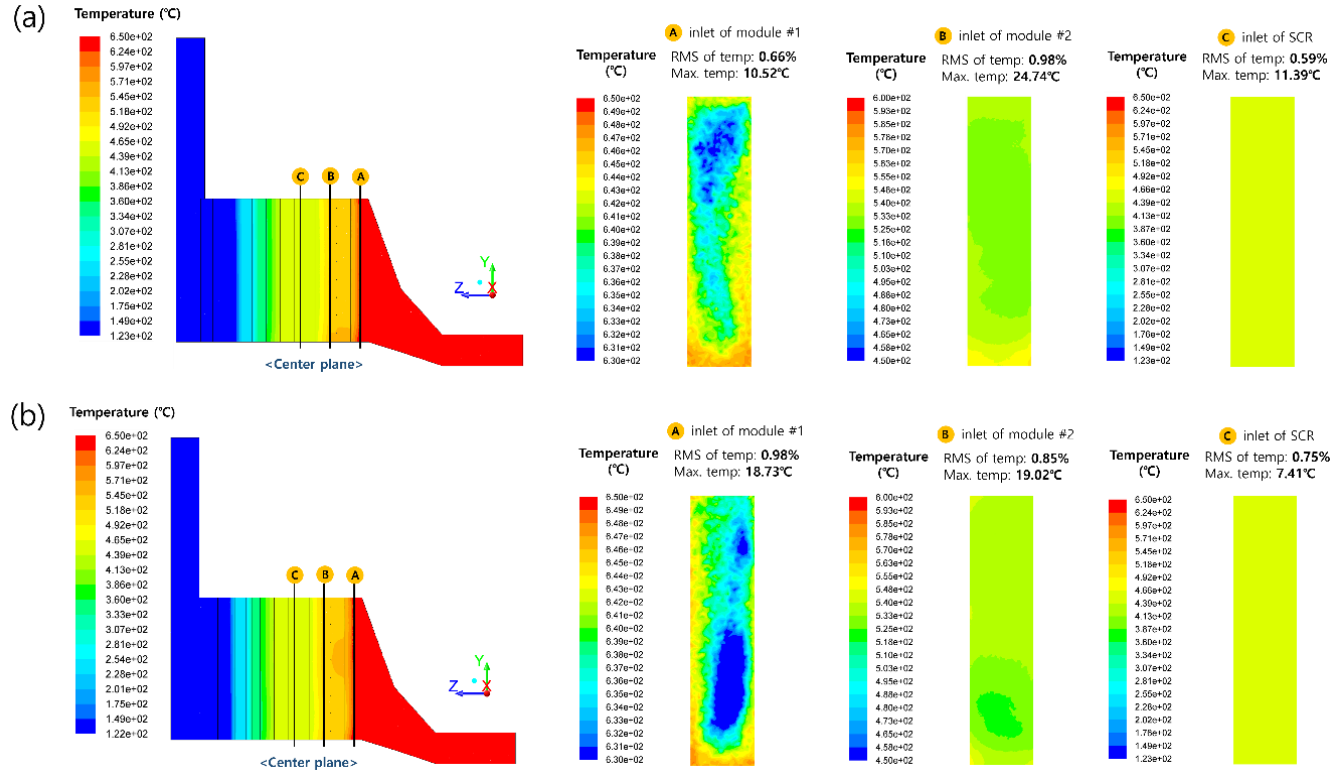

Figure 15. Temperature contours at the HRSG center plane, Module #1 inlet, Module #2 inlet, and SCR inlet for (a) θ = 30º; (b) θ = 40º

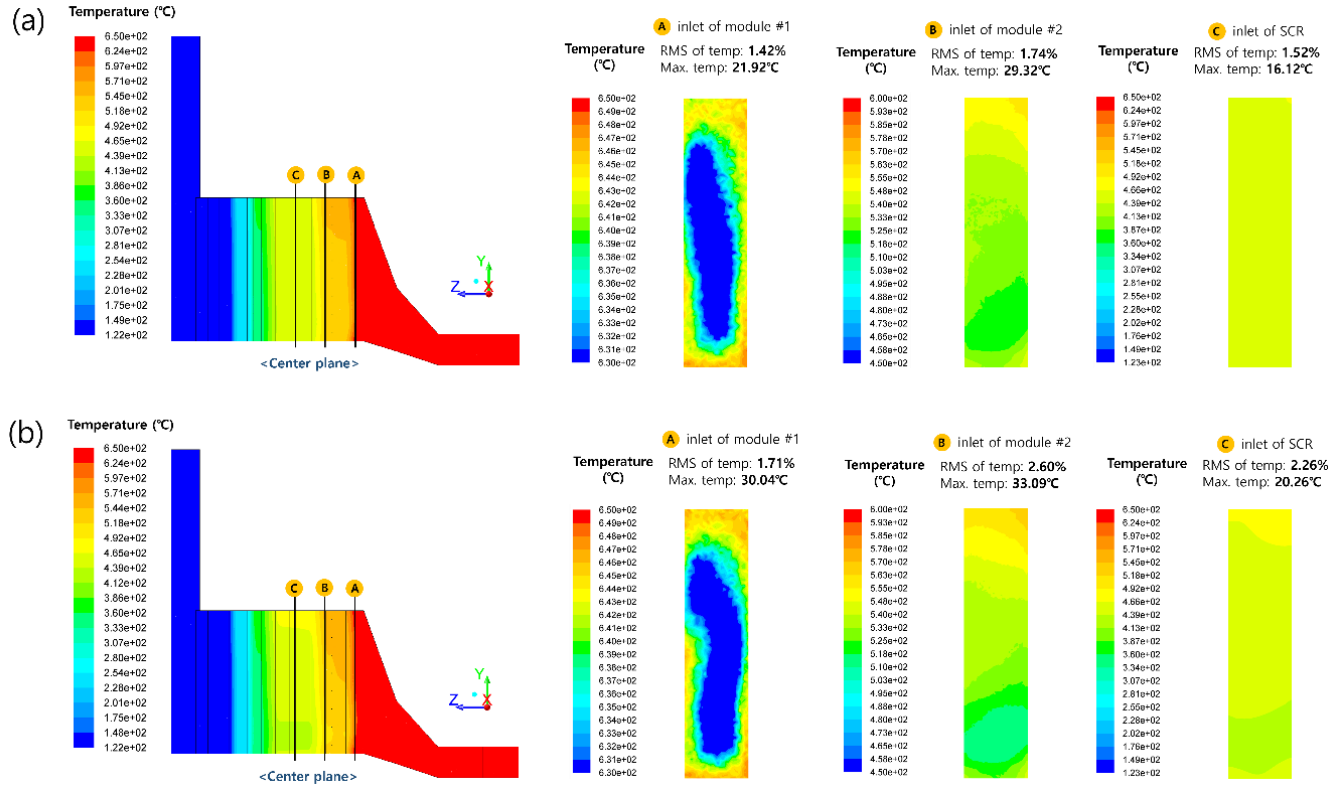

Figure 16. Temperature contours at the HRSG center plane, Module #1 inlet, Module #2 inlet, and SCR inlet for (a) θ = 50º; (b) θ = 60º

Table 6. RMS of z-Velocity Across Various Inspection Planes (Case-1)

Swirl Angle	Contents	Average z-Velocity (m/s)	Standard Deviation of z-Velocity (m/s)	RMS of z-Velocity
10°	Inlet of module #1	15.42	4.03	26.11%
	Inlet of module #2	13.68	0.43	3.16%
	Inlet of SCR	12.24	0.07	0.61%
20°	Inlet of module #1	15.41	3.47	22.53%
	Inlet of module #2	13.68	0.33	2.41%
	Inlet of SCR	12.24	0.05	0.43%
30°	Inlet of module #1	15.37	2.92	19.02%
	Inlet of module #2	13.67	0.21	1.52%
	Inlet of SCR	12.25	0.04	0.31%
40°	Inlet of module #1	15.33	2.98	19.44%
	Inlet of module #2	13.68	0.29	2.12%
	Inlet of SCR	12.26	0.07	0.59%
50°	Inlet of module #1	15.30	3.55	23.24%
	Inlet of module #2	13.69	0.45	3.25%
	Inlet of SCR	12.27	0.11	0.87%
60°	Inlet of module #1	15.29	4.56	29.82%
	Inlet of module #2	13.70	0.60	4.41%
	Inlet of SCR	12.27	0.14	1.17%

Table 7. RMS of z-Velocity Across Various Inspection Planes (Case-2)

Swirl Angle	Contents	Average z-Velocity (m/s)	Standard Deviation of z-Velocity (m/s)	RMS of z-Velocity
10°	Inlet of module #1	30.85	7.96	**25.80%**
	Inlet of module #2	27.31	0.91	**3.31%**
	Inlet of SCR	24.37	0.14	**0.59%**
20°	Inlet of module #1	30.83	6.89	**22.36%**
	Inlet of module #2	27.29	0.68	**2.51%**
	Inlet of SCR	24.39	0.11	**0.44%**
30°	Inlet of module #1	30.78	5.80	**18.86%**
	Inlet of module #2	27.28	0.50	**1.84%**
	Inlet of SCR	24.40	0.08	**0.34%**
40°	Inlet of module #1	30.70	5.67	**18.48%**
	Inlet of module #2	27.30	0.66	**2.43%**
	Inlet of SCR	24.41	0.14	**0.56%**
50°	Inlet of module #1	30.64	7.09	**23.14%**
	Inlet of module #2	27.31	0.95	**3.49%**
	Inlet of SCR	24.43	0.22	**0.88%**
60°	Inlet of module #1	30.62	9.10	**29.73%**
	Inlet of module #2	27.33	1.28	**4.69%**
	Inlet of SCR	24.44	0.29	**1.19%**

Table 8. Maximum Temperature Difference Across Various Inspection Planes (Case-1)

Swirl Angle	Contents	Average z-Velocity (m/s)	Standard Deviation of z-Velocity (m/s)	RMS of z-Velocity
10°	Inlet of module #1	30.85	7.96	25.80%
	Inlet of module #2	27.31	0.91	3.31%
	Inlet of SCR	24.37	0.14	0.59%
20°	Inlet of module #1	30.83	6.89	22.36%
	Inlet of module #2	27.29	0.68	2.51%
	Inlet of SCR	24.39	0.11	0.44%
30°	Inlet of module #1	30.78	5.80	18.86%
	Inlet of module #2	27.28	0.50	1.84%
	Inlet of SCR	24.40	0.08	0.34%
40°	Inlet of module #1	30.70	5.67	18.48%
	Inlet of module #2	27.30	0.66	2.43%
	Inlet of SCR	24.41	0.14	0.56%
50°	Inlet of module #1	30.64	7.09	23.14%
	Inlet of module #2	27.31	0.95	3.49%
	Inlet of SCR	24.43	0.22	0.88%
60°	Inlet of module #1	30.62	9.10	29.73%
	Inlet of module #2	27.33	1.28	4.69%
	Inlet of SCR	24.44	0.29	1.19%

Table 9. Maximum Temperature Difference Across Various Inspection Planes (Case-2)

Swirl Angle	Contents	Average Temperature (℃)	Maximum Temperature (℃)	Minimum Temperature (℃)	Maximum Difference (℃)
10°	Inlet of module #1	643.69	648.82	629.25	**14.44**
	Inlet of module #2	535.46	559.55	513.59	**24.09**
	Inlet of SCR	448.59	464.23	433.51	**15.64**
20°	Inlet of module #1	643.23	648.70	631.09	**12.14**
	Inlet of module #2	535.10	558.57	516.51	**23.47**
	Inlet of SCR	449.00	462.45	435.72	**13.45**
30°	Inlet of module #1	642.53	648.78	634.88	**7.66**
	Inlet of module #2	534.92	557.66	528.32	**22.74**
	Inlet of SCR	449.49	460.94	444.42	**11.45**
40°	Inlet of module #1	639.95	648.99	623.49	**16.46**
	Inlet of module #2	535.33	555.25	526.91	**19.92**
	Inlet of SCR	449.76	459.64	444.21	**9.88**
50°	Inlet of module #1	637.63	649.02	617.83	**19.80**
	Inlet of module #2	535.40	565.04	521.39	**29.64**
	Inlet of SCR	450.26	467.66	439.50	**17.41**
60°	Inlet of module #1	636.39	648.99	609.37	**27.03**
	Inlet of module #2	535.89	570.39	513.53	**34.50**
	Inlet of SCR	450.56	472.42	433.58	**21.85**

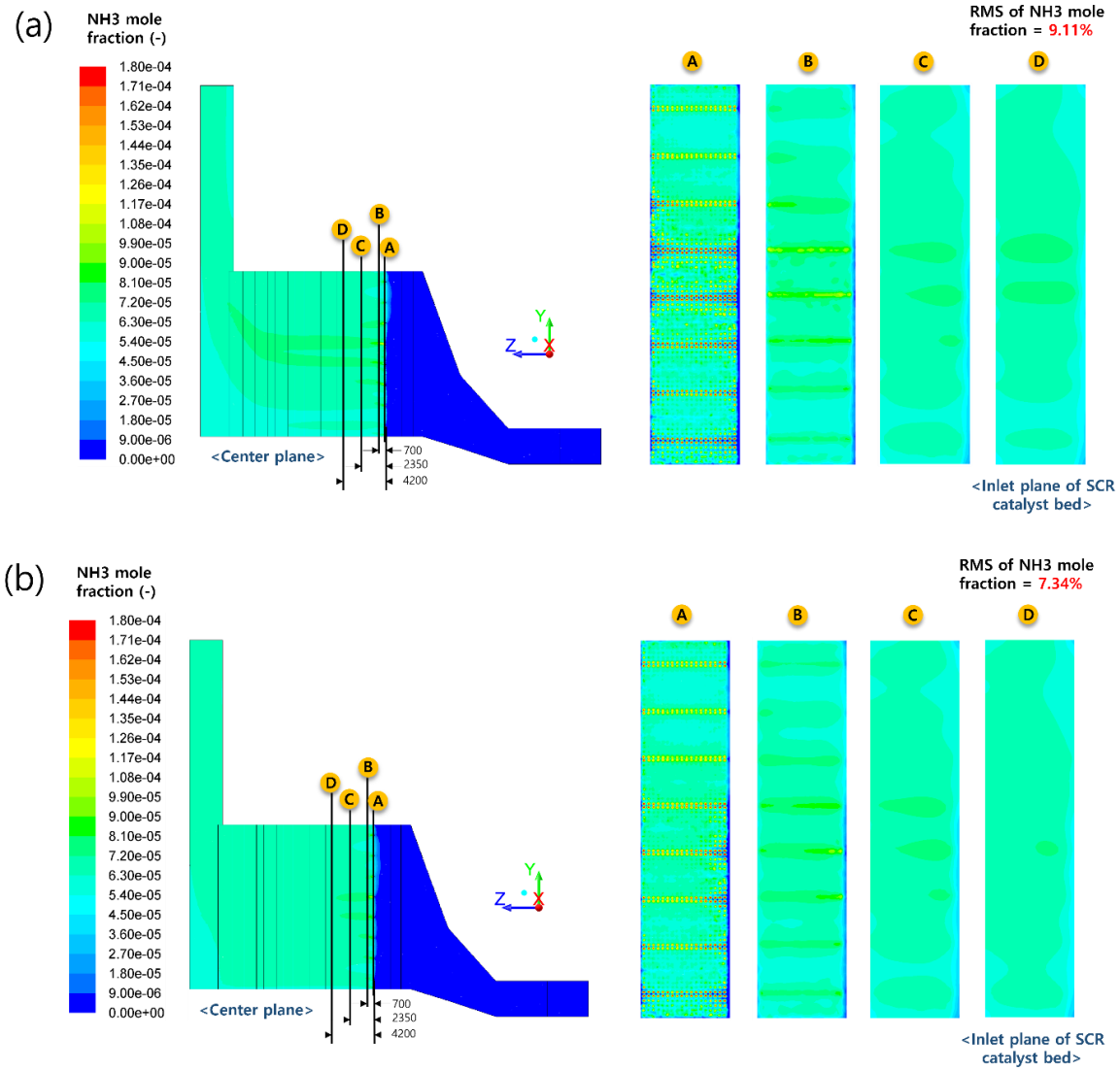

Figure 17. NH_3 mole fraction contours at the HRSG center plane, after AIG (a), Module #2 inlet, Module #2 outlet, and SCR inlet for (a) θ = 10º; (b) θ = 20º

Table 10 (Case-1) with RMS values showed the key points NH_3 distribution uniformity in the system while Table 11 (Case-2) provides additional data for the system.

Tables 10 combined with 11 showcase the relationship between rotating angles and mass flow values regarding NH_3 uniformity throughout the SCR device. The mixing effectiveness decreased when the simulation used low swirl angles (θ = 10°) and high swirl angles (θ = 60°) excessive swirl (θ = 60°) disrupted mixing, as reported in [16] and which produced increased values of RMS at the SCR inlet. Uniform distribution of NH_3 depends entirely on selecting the proper swirl angle because it ensures both effective SCR performance and emission standard compliance.

At θ = 30° the RMS of NH_3 mole fraction achieved its lowest values of 4.27% for Case-1 and 4.36% for Case-2. Eddy dissipation scales at θ = 30° reach an optimal range of 0.1 m that combines maximum NH_3 distribution with minimum surface wetting. Reagent homogenization follows turbulence timescales shorter than 0.5 seconds according to Gao *et al.* 2019 [9] study. When the system operates at θ = 10° or 60° inadequate turbulence results because it provides both insufficient mixing and unfavorable NH_3 stratification caused by excessive swirl.

3.4.1 RMS of NH_3 Mole Fraction

The Root Mean Square (RMS) of the NH_3 mole fraction was calculated to quantify the uniformity of NH_3 distribution at various inspection planes. As illustrated in Figure 20, the RMS values reveal that the lowest RMS value occurs at θ = 30° for both Case-1 and Case-2, while the highest RMS values are showed at θ = 10° (9.11% for Case-1, 9.20% for Case-2) and θ = 60° (9.53% for Case-1, 9.64% for Case-2).

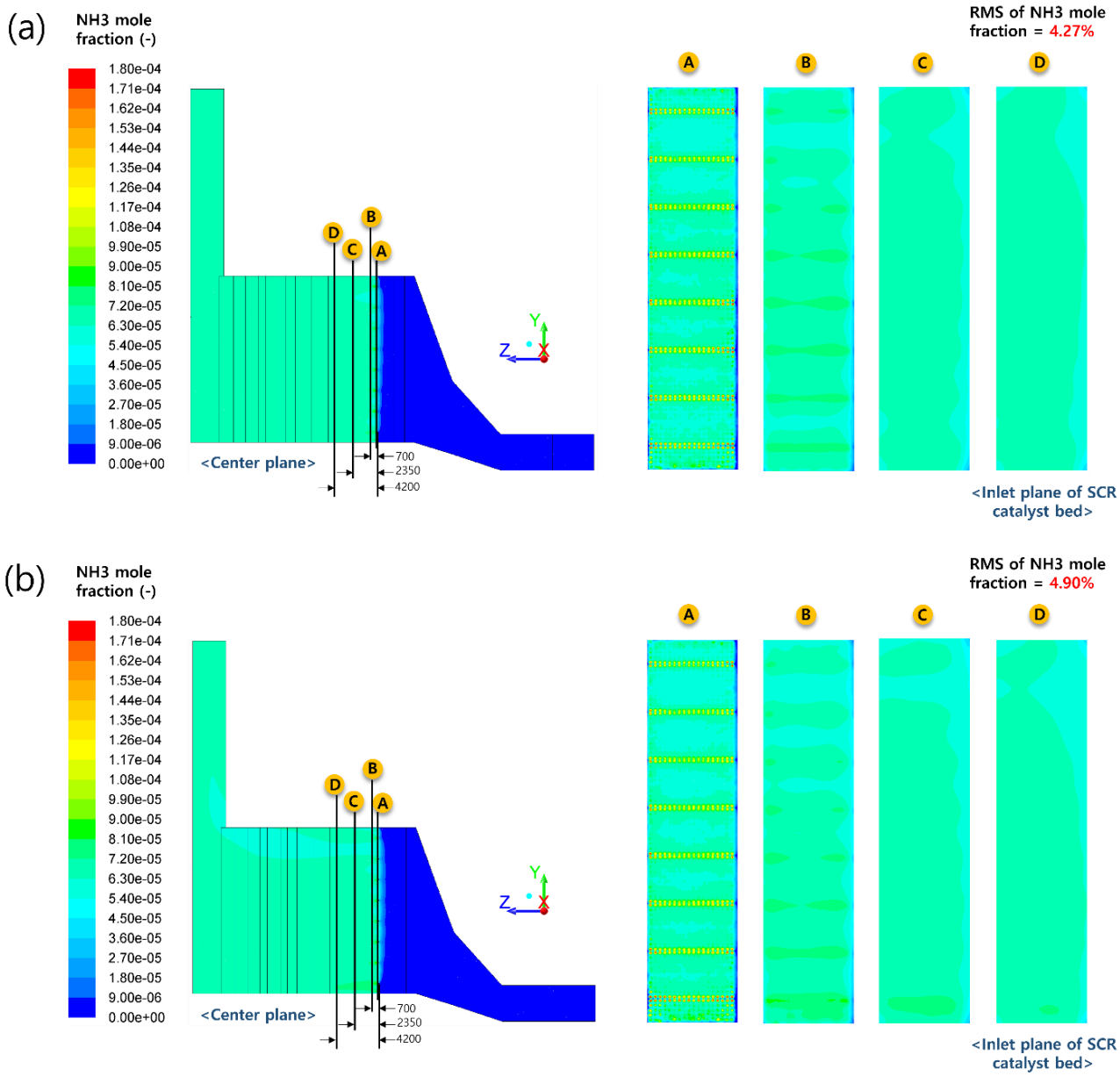

Figure 18. NH_3 mole fraction contours at the HRSG center plane, after AIG (a), Module #2 inlet, Module #2 outlet, and SCR inlet for (a) θ = 30º; (b) θ = 40º

3.4.2 Interpretation of Figure 20

The NH_3 mixing uniformity in an SCR system depends on swirl angle at both 350 kg/s and 700 kg/s mass flow rates as shown in Figure 20. According to the plot data when using a swirl angle of 30° the system displays optimal NH_3 distribution because it reaches the lowest RMS values of 4.27% at 350 kg/s and 4.36% at 700 kg/s which satisfy the industrial requirement [8, 15, 23] of below 5% RMS. The standard deviation error bars demonstrate that unstable mixing through excessive or insufficient turbulence occurs at angles 10° and 60° because RMS exceeds 9%. The provided data shows flow rate variations result in minimal alterations of RMS values while swirl angle optimization stands as the primary factor for promoting uniform NH_3 distribution. The numerical simulation data [9] confirms that a 30° swirl angle represents the optimal design for SCR systems because it provides efficient NOx reduction and low ammonia slip during normal operational conditions.

3.4.3 Validation of Computational Results

The calculated numerical data matches both industrial requirements and findings reported in the literature. The results presented in Table 12 demonstrate that uniform NH_3 distribution (RMS = 4.27-4.36%) becomes possible with an optimal θ = 30° swirl angle and thereby fulfills the strict <5% standard established in and Sohn *et al.* 2021 [8], Li *et al.* 2009 [23] and Ye. 2018 [15]. The uniform mixing efficiency achieved at this level guarantees both high NOx reduction capabilities and low ammonia slip performance needed for industrial SCR systems.

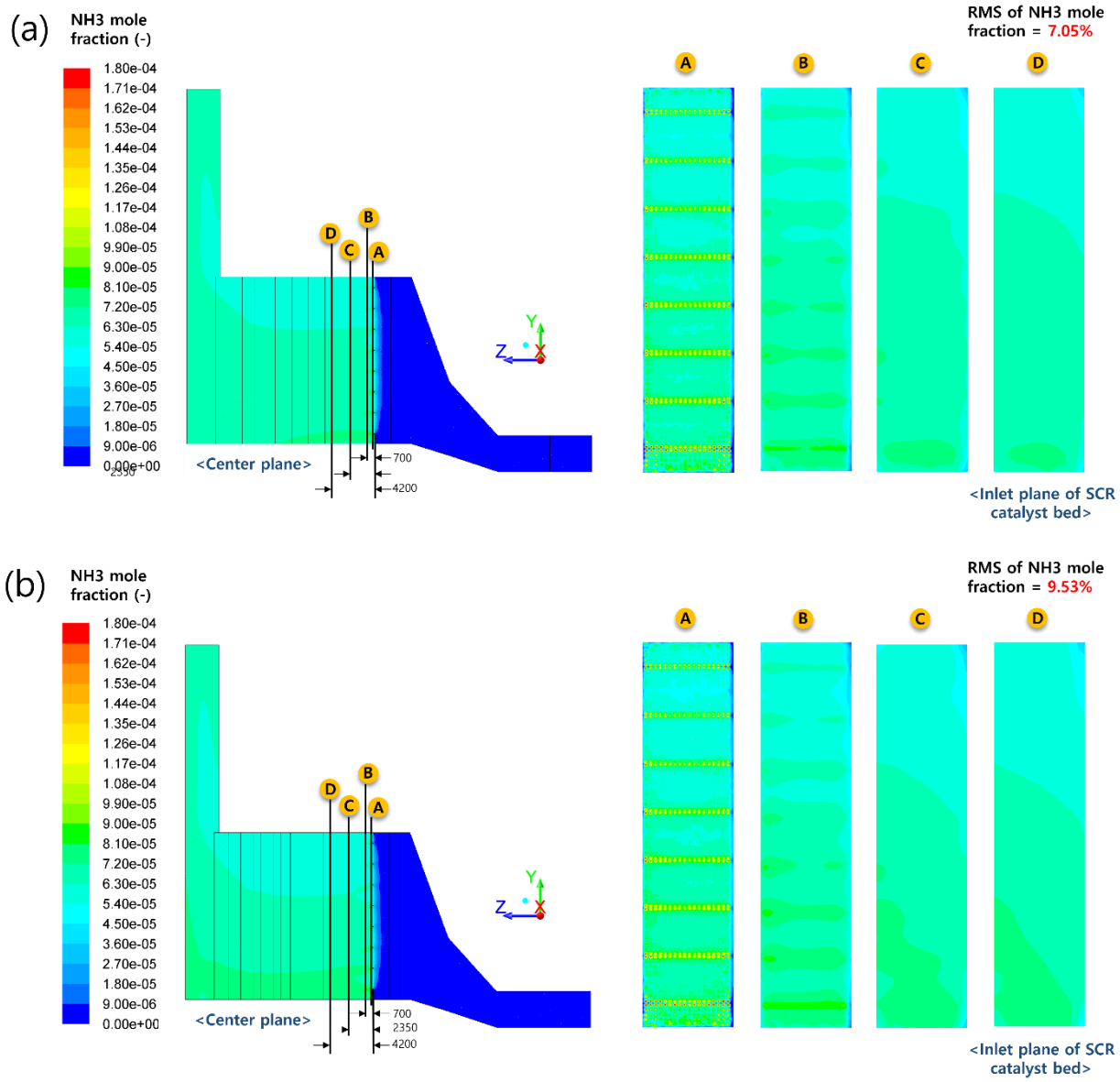

Figure 19. NH_3 mole fraction contours at the HRSG center plane, after AIG (a), Module #2 inlet, Module #2 outlet, and SCR inlet for (a) θ = 50º; (b) θ = 60º

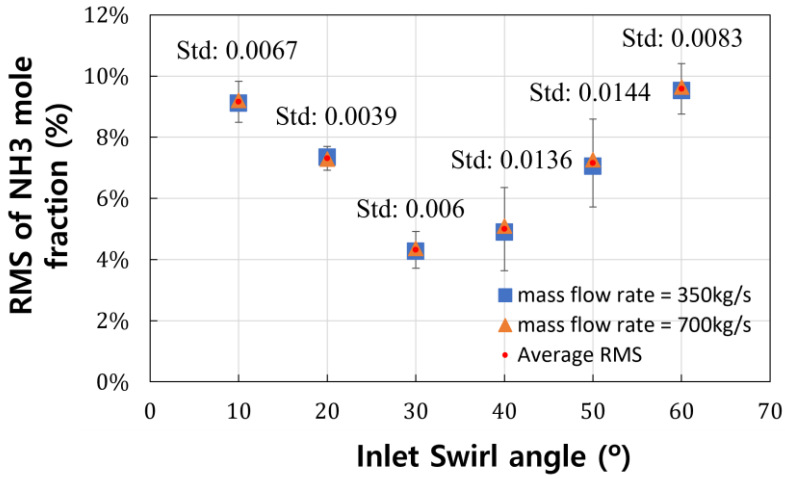

Figure 20. Illustrates the Root Mean Square (RMS) of NH_3 mole fraction as a function of swirl angle for two mass flow rates: m = 350 kg/s and m = 700 kg/s.

Table 10. RMS of NH_3 Mole Fraction Across Various Inspection Planes and Inlet of SCR Catalyst Bed (Case-1)

Swirl Angle	Contents	Average NH_3 Mole Fraction (-)	Standard Deviation of NH_3 Mole Fraction (-)	RMS of NH_3 Mole Fraction
10°	A	6.56E-05	5.08E-05	77.39%
	Inlet of module #2	6.54E-05	1.12E-05	17.18%
	Outlet of module #2	6.52E-05	6.95E-06	10.66%
	Inlet of SCR	6.52E-05	5.94E-06	9.11%
20°	A	6.57E-05	3.82E-05	58.12%
	Inlet of module #2	6.53E-05	9.84E-06	15.06%
	Outlet of module #2	6.52E-05	5.80E-06	8.89%
	Inlet of SCR	6.52E-05	4.79E-06	7.34%
30°	A	6.59E-05	2.65E-05	40.23%
	Inlet of module #2	6.53E-05	7.22E-06	11.05%
	Outlet of module #2	6.52E-05	3.53E-06	5.41%
	Inlet of SCR	6.52E-05	2.79E-06	4.27%
40°	A	6.60E-05	2.52E-05	38.19%
	Inlet of module #2	6.53E-05	6.74E-06	10.31%
	Outlet of module #2	6.52E-05	3.62E-06	5.55%
	Inlet of SCR	6.52E-05	3.20E-06	4.90%
50°	A	6.63E-05	2.51E-05	37.87%
	Inlet of module #2	6.54E-05	7.44E-06	11.38%
	Outlet of module #2	6.52E-05	4.97E-06	7.62%
	Inlet of SCR	3.93E-05	2.77E-06	7.05%
60°	A	6.64E-05	2.54E-05	38.19%
	Inlet of module #2	6.54E-05	8.53E-06	13.04%
	Outlet of module #2	6.52E-05	6.54E-06	10.02%
	Inlet of SCR	3.93E-05	3.75E-06	9.53%

The flow field data indicates outstanding inlet velocity consistency through the SCR because z-velocity RMS deviates below 1.19% from the recommended values reported by Sohn *et al.* 2021 [8] and Ye. 2018 [15]. Our newly designed HRSG attains superior flow

conditioning capabilities because of the correct module structure combined with optimal diffuser design.

The thermal management system achieves temperature stability within a range of ±7.41 - 9.88 °C at θ = 40° thus maintaining safe operating conditions as cited by Ye *et al.* 2021 [5] and Haifeng. 2009 [24] for catalyst performance. Variable mass flow rates from 350 to 700 kg/s do not affect the system's ability to keep temperatures within specified limits according to the design requirements.

Turbulence characteristics obtained from the designated swirl angle (θ = 30°) fit within the findings reported by Gao *et al.* 2019 [9] investigations of SCR mixing dynamics. The studies used different mixer setups but demonstrated similar turbulence kinetic energy levels and mixing timescales because both test series shared equivalent physical processes.

A thorough validation ensures our computational model correctly predicts all the following performance aspects adequately:

1 The NH_3/NOx mixing operations match requirements established by the industry.

2 The uniform flow distribution guarantees complete catalyst utilization.

3 Thermal stability preventing catalyst deactivation.

4 The swirling effects comply with established turbulence principles.

Table 11. RMS of NH_3 Mole Fraction Across Various Inspection Planes and Inlet of SCR Catalyst Bed (Case-2)

Swirl Angle	Contents	Average NH_3 Mole Fraction (-)	Standard Deviation of NH_3 Mole Fraction (-)	RMS of NH_3 Mole Fraction
10°	A	3.27E-05	2.48E-05	75.91%
	Inlet of module #2	3.28E-05	5.69E-06	17.18%
	Outlet of module #2	3.27E-05	3.55E-06	10.84%
	Inlet of SCR	3.27E-05	3.01E-06	9.20%
20°	A	3.29E-05	1.80E-05	54.67%
	Inlet of module #2	3.28E-05	4.87E-06	14.84%
	Outlet of module #2	3.27E-05	2.89E-06	8.81%
	Inlet of SCR	3.28E-05	2.39E-06	7.29%
30°	A	3.30E-05	1.32E-05	40.10%
	Inlet of module #2	3.28E-05	3.71E-06	11.31%
	Outlet of module #2	3.28E-05	1.83E-06	5.60%
	Inlet of SCR	3.28E-05	1.43E-06	4.36%
40°	A	3.30E-05	1.27E-05	38.41%
	Inlet of module #2	3.28E-05	3.60E-06	10.96%
	Outlet of module #2	3.28E-05	1.94E-06	5.91%
	Inlet of SCR	3.28E-05	1.67E-06	5.90%
50°	A	3.32E-05	1.18E-05	35.67%
	Inlet of module #2	3.28E-05	3.74E-06	11.38%
	Outlet of module #2	3.28E-05	2.57E-06	7.83%
	Inlet of SCR	3.28E-05	2.38E-06	7.26%
60°	A	3.33E-05	1.19E-05	35.81%
	Inlet of module #2	3.29E-05	4.26E-06	12.95%
	Outlet of module #2	3.28E-05	3.32E-06	10.12%
	Inlet of SCR	3.28E-05	3.16E-06	9.64%

Table 12. Comparative Analysis of SCR Performance: Present Study vs. Prior Research

Parameters	Present Study Case-1 and Case-2	Literature Benchmark	Reference	Compliance
NH_3 RMS uniformity	4.27-4.36%	<5% (industrial standard)	Sohn *et al*. 2021 [8], Ye. 2018 [15] and Li *et al.* 2009 [23]	Satisfied
Velocity RMS	<1.19%	<15% (catalyst requirement)	Sohn *et al*. 2021 [8] and Ye. 2018 [15]	Satisfied
Maximum Temperature deviation	±7.41-9.88°C	±10°C (operational limit)	Ye *et al.* 2021 [5] and Haifeng. 2009 [24]	Satisfied
Mixing efficiency	θ=30° optimum	Matches turbulence criteria	Gao *et al.* 2019 [9]	Satisfied

Our numerical approach demonstrates reliability thanks to multiple independent work from Ye *et al.* 2021 [5], Sohn *et al.* 2021 [8], Gao *et al.* 2019 [9], Ye. 2018 [15], Li *et al.* 2009 [23] and Haifeng. 2009 [24]. These studies also validate the practically address the optimized design for industrial applications.

4. Conclusion

This computational simulation method evaluated in detail how swirl angle settings and mass flow rates affect the distribution quality of ammonia in Selective Catalytic Reduction (SCR) systems. A swirl angle of 30° demonstrates the best NH_3 distribution according to the study which maintains uniform distribution levels at or below 5% RMS requirements for SCR NOx reduction results. The 30° swirl configuration proved better than both lower (10°-20°) and higher (40°-60°) angles because it created necessary turbulence and achieved flow stability. Under different operating conditions the system demonstrated continuous performance for both mass flow rates of 350 kg/s and 700 kg/s thus establishing the HRSG design's operational reliability. When using the 40° swirl angle the system achieved optimal thermal management by sustaining SCR inlet temperature uniformity between ±7.41-9.88°C making it essential for both catalyst durability and reaction effectiveness.

The research findings enable productive decisions in SCR systems design together with operational system optimization. The application of a 30° swirl angle serves as a practical method which enhances NH3 and NOx mixing efficiency without generating excessive ammonia slip during industrial operations. The steady performance observed at different flow rates ensures the SCR system works reliably under power plant load change conditions. Through its methodological approach this study builds reliable CFD software as an alternative to experimental testing procedures when optimizing SCR functionality. The analysis of dynamic swirl angle control methods with real-time control systems through machine learning innovations should be studied to optimize SCR performance in transient operations.

Nomenclature

Latin Symbols

A = Area [m^2]

A_{SP} = Specific surface area [m^2/m^3]

C_1, C_2, C_3 = Turbulence model constants [-]

C_p = Heat capacity [$j/kg.k$]

D = Mass diffusion coefficient [m^2/s]

D_{ij} = Viscous resistance coefficient matrix [-]

C_{ij} = Inertial resistance coefficient matrix [-]

E = Energy sink rate [W]

G_k, G_b = Turbulence kinetic energy generation terms [-]

h = Heat transfer coefficient [$W/(m^2.K)$]

J_i = Diffusion flux of species ii [$Kg/(m^2.s)$]

k = Turbulence kinetic energy [m^2/s^2]

m = Mass flow rate [kg/s]

MW_i = Molecular weight of species i [$kg/kmol$]

p = Static pressure [Pa]

P_{rt} = Turbulent Prandtl number [-]

R_i = Net production rate of species i [$kg/(m^3.s)$]

S_i = Source term for species i [$kg/(m^3.s)$]

S_e = Energy source term [W/m^3]

S_{ct} = Turbulent Schmidt number [-]

T = Temperature [K or °C]

t = Time [s]

u, v, w = Velocity components [m/s]

V = Volume [m^3]

x_i = Variable value at sampling point i [-]

Y_i = Mass fraction of species i [-]

Greek Symbols

θ = Swirl angle [°]

ϵ = Turbulence dissipation rate [m^2/s^3]

μ = Dynamic viscosity [$kg/(m.s)$]

μ_t = Turbulent viscosity [$kg/(m.s)$]

ρ = Density [kg/m^3]

$\sigma_k, \sigma_\epsilon$ = Turbulent Prandtl numbers for k and ϵ [-]

Abbreviations

AIG = Ammonia Injection Grid

CFD = Computational Fluid Dynamics

DPM = Discrete Phase Model

GT = Gas Turbine

HRSG = Heat Recovery Steam Generator

LES = Large Eddy Simulation

NH_3 = Ammonia

NOx = Nitrogen Oxides

RANS = Reynolds-Averaged Navier-Stokes

RMS = Root Mean Square

SCR = Selective Catalytic Reduction

References

[1] Z. Zhou, J. Chang, X. Wang, Large Eddy Simulation of Hydrodynamics and DeNO$_x$ Process in a Coal-Fired Power Plant SCR System. Journal of Environmental Management, 320, (2022) 115800. https://doi.org/10.1016/j.jenvman.2022.115800

[2] C. Zheng, X. Li, J. Li, J. Duan, H. Wu, F. Zhu, Investigation on the Ammonia Emission Characteristics in Coal-Fired Power Plants of China. Fuel, 314, (2022) 123046. https://doi.org/10.1016/j.fuel.2021.123046

[3] B. Hu, C. Chen, S. Jiang, X. Liu, Q. Dai, Investigating the Optimization Design of Internal Flow Fields Using a Selective Catalytic Reduction Device and Computational Fluid Dynamics. Energies, 15(4), (2022) 1451. https://doi.org/10.3390/en15041451

[4] J. An X. Luo, Numerical Simulation of Ash Erosion in the Selective Catalytic Reduction Catalyst of Power Plant Boiler. Energy Reports, 8, (2022) 1313–1321. https://doi.org/10.1016/j.egyr.2021.11.169

[5] M. Ye, F. Qian, Y. Gao, J. Lu, Y. Han, N. Huang, B. Xu, H. Wu, CFD Analysis of Influencing Factors on SCR Denitration Efficiency of Sintering Flue Gas Based on Response Surface Methodology. Atmospheric Pollution Research, 12(7), (2021) 101107. https://doi.org/10.1016/j.apr.2021.101107

[6] M.G. Kim, D.C. Seo, H.T. Chung, A CFD Study on Flow Control of Ammonia Injection for Denitrification Processes of SCR Systems in Coal-Fired Power Plants. Energies, 14(5), (2021) 1352. https://doi.org/10.3390/en14051352

[7] G. Liu, W. Bao, W. Zhang, D. Shen, Q. Wang, C. Li, K. H. Luo, An Intelligent Control of NH_3 Injection for Optimizing the NOx/ NH_3 Ratio in SCR System. Journal of the Energy Institute, 92(5), (2019) 1262–1269. https://doi.org/10.1016/j.joei.2018.10.008

[8] J. Sohn, I. S. Hwang, J. Hwang, Improvement of Ammonia Mixing in an Industrial Scale Selective Catalytic Reduction De-NO$_x$ System of a Coal-Fired Power Plant: A Numerical Analysis. Process Safety and Environmental Protection, 147, (2021) 334–345. https://doi.org/10.1016/j.psep.2020.09.043

[9] X. Gao, B. Wang, X. Yuan, S. Lei, Q. Qu, C. Ma, L. Sun, Optimal Design of Selective Catalyst Reduction Denitrification System Using Numerical Simulation. Journal of Environmental Management, 231, (2019) 909–918. https://doi.org/10.1016/j.jenvman.2018.10.060

[10] C. Zhang, G. Liu, X. Zhang, A. Song, D. Xu, X. Jiang, C. Gong, X. Zhou, Q. Gong, D. Shen, "A Partitioned Dynamic Ammonia Injection Strategy Based on Real-Time NO$_x$ Flux Distribution Characteristics in an SCR System. Fuel, 381, (2025) 133711. https://doi.org/10.1016/j.fuel.2024.133711

[11] Y. Chen, H. Xiao, C. Hong, Y. Ma, Y. Ni, Application of a Composite Parameter-Driven TimeMixer Model for Multi-Step Prediction of NO$_x$ at the SCR Inlet of a 660 MW Boiler, Fuel, 386, (2025) 134060. https://doi.org/10.1016/j.fuel.2024.134060

[12] Z. Dong, W. Jiang, Z. Wu, X. Zhao, M. Sun, Prediction of NO$_x$ Emission from SCR Zonal Ammonia Injection System of Boiler Based on Ensemble Incremental Learning. Energy, 319, (2025) 135049. https://doi.org/10.1016/j.energy.2025.135049

[13] W.P. Adamczyk, B. Isaac, J. Parra-Alvarez, S.T. Smith, D. Harris, J.N. Thornock, M. Zhou, P.J. Smith, R. Żmuda, Application of LES-CFD for Predicting Pulverized-Coal Working Conditions after Installation of NOx Control System. Energy, 160, (2018) 693–709. https://doi.org/10.1016/j.energy.2018.07.031

[14] Y. Gao, Q. Liu, L. Bian, Numerical Simulation and Optimization of Flow Field in the SCR Denitrification System on a 600 MW Capacity Units. Energy Procedia, 14, (2012) 370–375. https://doi.org/10.1016/j.egypro.2011.12.944

[15] X. Ye, Research and Application of Multi-Dimension Numerical Simulation Optimization for SCR DeNOx Flow Field. IOP Conference Series: Earth and Environmental Science, 113, (2018) 012181. https://doi.org/10.1088/1755-1315/113/1/012181

[16] L. Tan, P. Feng, S. Yang, Y. Guo, S. Liu, Z. Li, CFD Studies on Effects of SCR Mixers on the Performance of Urea Conversion and Mixing of the Reducing Agent. Chemical Engineering and Processing - Process Intensification, 123, (2018) 82–88. https://doi.org/10.1016/j.cep.2017.11.003

[17] J. Zhu, Z. Ye, D. Gong, Q. Wang, Q. Luo, Ammonia Distribution Characteristics at the Selective Catalytic Reduction Reactor Inlet with Linear Partitioning. iScience, 28(1), (2025) 111588. https://doi.org/10.1016/j.isci.2024.111588

[18] H.S. Choi, S.J. Kim, K.T. Kim, Enhancement of Turbulent Scalar Mixing and Its Application by a Multihole Nozzle in Selective Catalytic Reduction of NO_x. Journal of Material Cycles and Waste Management, 10(1), (2008) 1–6. https://doi.org/10.1007/s10163-007-0190-0

[19] D. Yongqiang, M. Zhongming, M. Yijun, L. Nianping, Y. Guoming, Numerical Simulations of SCR DeNO$_x$ System for a 660MW Coal-Fired Power Station. E3S Web Conference International Conference on Energy Materials and Environment Engineering (ICEMEE 2018), 38, (2018) 04009. https://doi.org/10.1051/e3sconf/20183804009

[20] Z. Lei, C. Wen, B. Chen, Optimization of Internals for Selective Catalytic Reduction (SCR) for NO Removal. Environmental Science & Technology, 45(8), (2011) 3437–3444. https://doi.org/10.1021/es104156j

[21] F. Sadeghi, B. Tirandazi, A. Khalili-Garakani, S. Nasseri, R. Nabizadeh Nodehi, N. Mostoufi, Investigating the Effect of Channel Geometry on Selective Catalytic Reduction of NO_x in Monolith Reactors. Chemical Engineering Research and Designvol, 118, (2017) 21–30. https://doi.org/10.1016/j.cherd.2016.12.003

[22] S. Gourari, F. Mebarek-Oudina, O.D. Makinde, M. Rabhi, Numerical Investigation of Gas-Liquid Two-Phase Flows in a Cylindrical Channel. Defect and Diffusion Forum, 409, (2021) 39-48. https://doi.org/10.4028/www.scientific.net/DDF.409.39

[23] M. Li, H. Yan, J. Zhou, Numerical Simulation and Optimization of Flow Field in the SCR Denitrification System, proceeding of the 2009 International Conference on Energy and Environment Technology, IEEE, (2009) 415–418. https://doi.org/10.1109/ICEET.2009.565

[24] C. Haifeng, (2009) Research and Application of Numerical Calculation Methods in SCR DeNOx Reactor & Duct Design. Proceeding of the 11th International Conference on Electrostatic Precipitation, Springer, Berlin. https://doi.org/10.1007/978-3-540-89251-9_126

[25] M. Guo, J. Gao, K. Niu, Y. Huang, M. Xiao, Y. Zhao, S. Cui, W. Ye, B. Liu, SCR Performance and Mechanism Study with Multiple Poisoning Gases on CeO_x Promoted V_2O_5-WO_3/TiO_2 Monolithic Honeycomb Catalyst of NO_x Removal. Separation and Purification Technology, 363, (2025) 132087. https://doi.org/10.1016/j.seppur.2025.132087

[26] Y. Wang, X. Ren, K. Li, Y. Shao, Y. Zhou, M. Zhao, C. Liu, Y. Liu, X. Liu, A. Dong, H. Wu, M. Wang, L. Meng, W. Zhang, Z. Li, and Q. Liu, "Enhanced NH_3-SCR Performance of High-Silica MER Zeolite via Template Synthesis. Fuel, 392, (2025) 134818. https://doi.org/10.1016/j.fuel.2025.134818

[27] S. Xiao, C. Li, X. Zheng, L. Li, J. Si, X. Shu, X. Zeng, Application of a Low-Cost and High-Efficiency Polymer Non-Catalytic Reduction Technology for NO_x Removal in Waste-to-Energy Plant. Journal of Environmental Sciences, In Press, Journal Pre-proof, (2025). https://doi.org/10.1016/j.jes.2025.01.026

[28] F. Lakhfif, Z. Nemouchi, F. Mebarek-Oudina, Numerical Investigation of the Different Spray Combustion Models under Diesel Condition. International Journal of Applied Engineering Research, 11(18), (2016) 9393-9399. https://doi.org/10.26524/ijpefs1945

[29] H. Tang, G. Yao, Z. Wang, J. Yang, X. Han, L. Sun, and Z. Xu, Study on Low-Load Combustion Characteristics of a 600 MW Power Plant Boiler with Self-Sustaining Internal Combustion Burners. Applied Thermal Engineering, 267, (2025) 125859. https://doi.org/10.1016/j.applthermaleng.2025.125859

[30] H. Wang, Y. Yan, Z. Li, Z. Cao, Y. Fu, Z. Zhou, D. Zhao, Carbon Mitigation Potential and Economic Benefits of Biomass Co-Firing in Coal-Fired Power Plants: A Case Study in Nanjing, China. Energy, 314, (2025) 134262. https://doi.org/10.1016/j.energy.2024.134262

[31] Y. Xu, Y. Zhang, J. Wang, J. Yuan, Application of CFD in the Optimal Design of a SCR–DeNO$_x$ System for a 300 MW Coal-Fired Power Plant. Computers & Chemical Engineering, 49, (2013) 50–60. https://doi.org/10.1016/j.compchemeng.2012.09.014

[32] Y. Xu, Y. Zhang, F. Liu, W. Shi, J. Yuan, CFD Analysis on the Catalyst Layer Breakage Failure

of an SCR-DeNO$_x$ System for a 350MW Coal-Fired Power Plant. Computers & Chemical Engineering, 69, (2014) 119–127. https://doi.org/10.1016/j.compchemeng.2014.07.012

[33] X. Liu, H. Tan, Y. Wang, F. Yang, H. Mikulčić, M. Vujanović, N. Duić, Low NO$_x$ Combustion and SCR Flow Field Optimization in a Low Volatile Coal Fired Boiler. Journal of Environmental Management, 220, (2018) 30–35. https://doi.org/10.1016/j.jenvman.2018.05.009

[34] O.T. Kaario, V. Vuorinen, L. Zhu, M. Larmi, R. Liu, Mixing and Evaporation Analysis of a High-Pressure SCR System Using a Hybrid LES-RANS Approach. Energy, 120, (2017) 827–841. https://doi.org/10.1016/j.energy.2016.11.138

[35] F. Mebarek-Oudina, H. Laouira, A.K. Hussein, M. Omri, A. Abderrahmane, L. Kolsi, U. Biswal, Mixed Convection inside a Duct with an Open Trapezoidal Cavity Equipped with Two Discrete Heat Sources and Moving Walls. Mathematics, 10(6), (2022) 929. https://doi.org/10.3390/math10060929

[36] Y. Ding, S. Yinbiao, W. Qingyun, Z. Hao, Y. Xinglian, (2016) Mixing Enhancement of Ammonia and Flue Gas in the SCR DeNOx System. Clean Coal Technology and Sustainable Development. Springer, Singapore. https://doi.org/10.1007/978-981-10-2023-0_77

[37] L. Han, S. Cai, M. Gao, J. Hasegawa, P. Wang, J. Zhang, L. Shi, D. Zhang, Selective Catalytic Reduction of NO$_x$ with NH$_3$ by Using Novel Catalysts: State of the Art and Future Prospects. Chemical Reviews, 119(19), (2019) 10916–10976. https://doi.org/10.1021/acs.chemrev.9b00202

[38] R.K.C. Amadi, D. Charles, Efficiency Analysis of the Turbine using Calorific Value Parameters for a 10 Megawatt Gas Turbine. International Research Journal of Multidisciplinary Technovation, 3(4), (2021) 59–66. https://doi.org/10.34256/irjmt2147

[39] D. Anand, S. Vellingiri, Design and Analysis of Exhaust Manifold. International Research Journal of Multidisciplinary Technovation, 2(6), (2020) 1–8. https://doi.org/10.34256/irjmt2061

[40] F. Gholami, M. Tomas, Z. Gholami, M. Vakili, Technologies for the Nitrogen Oxides Reduction from Flue Gas: A Review. Science of the Total Environment, 714, (2020) 136712. https://doi.org/10.1016/j.scitotenv.2020.136712

[41] G. Liu, Y. Cui, J. Ji, D. Shen, Q. Wang, C. Li, K. H. Luo, A Technical Method to Improve NO$_x$/ NH$_3$ Mixing Ratio in SCR System and Its Engineering Applications. Journal of the Energy Institute, 92(6), (2019) 1757–1764. https://doi.org/10.1016/j.joei.2018.12.005

[42] Z. Chen, Q. Liu, H. Liu, T. Wang, Recent Advances in SCR Systems of Heavy-Duty Diesel Vehicles—Low-Temperature NO$_x$ Reduction Technology and Combination of SCR with Remote OBD. Atmosphere, 15(8), (2024) 997. https://doi.org/10.3390/atmos15080997

[43] ANSYS, Inc., ANSYS Fluent User's Guide, Release 19.0, ANSYS, Inc., Canonsburg, PA, 2020.

Authors Contribution Statement

Gutti Lokesh Kalyan; Conceptualization, Methodology, Investigation, Data collection, Data Curation, Writing original manuscript. Rajendra Singh Rajput: Formal Analysis, Data Curation, Writing original manuscript. Sunkara Srinivasa Rao: Formal Analysis, Writing, Review & Editing. Mukesh Kumar Pandey: Formal Analysis, Writing, Review & Editing. All the authors read approved the final version of the manuscript.

Funding

The authors declare that no funds, grants or any other support were received during the preparation of this manuscript.

Competing Interests

The authors declare that there are no conflicts of interest regarding the publication of this manuscript.

Data Availability

The data supporting the findings of this study can be obtained from the corresponding author upon reasonable request.

Has this article screened for similarity?

Yes

About the License